RADAR IMAGING OF VOLCANIC FIELDS AND SAND DUNE FIELDS: IMPLICATIONS FOR VOIR*

C. Elachi, R. Blom, M. Daily, T. Farr, and R. S. Saunders

Earth and Space Science Division
Jet Propulsion Laboratory
Pasadena, California

ABSTRACT

A number of volcanic fields and sand dune fields in the western part of North America have been studied using aircraft and Seasat SAR images and Landsat images. The objective of the study was to assess the capability of radars with different characteristics (i.e., frequency, polarization and look-angles) to identify and map different volcanic features, lava flows and sand dune types. It was concluded that (1) volcanic features which have a relatively large topographic expression (i.e., cinder cones, collapse craters, calderas, etc.) are easily identified; (2) lava flows of different ages can be identified, particularly on the L-band images; and (3) sand dunes are clearly observed and their extent and large-scale geometric characteristics determined, provided the proper imaging geometry exists.

I. INTRODUCTION

Airborne imaging radars have been used, over the last decade, as a major source of information for geologic mapping in regions of the world where heavy vegetation and extensive cloud cover limit the usefulness of visible and IR sensors. Radar has, in fact, provided the only practical geological reconnaissance exploration technique in those regions of the world that are almost perpetually cloud covered. Many countries in the equatorial regions, such as Brazil, Nigeria, Togo and Indonesia, have conducted large-scale radar mapping programs and obtained accurate maps of vast areas that were formerly almost unknown and largely unmapped (e.g., MacDonald, 1969). Imaging radars have also been used over cloud-free regions to obtain complementary information to optical imaging sensors by providing surface reflectivity data in a different region of the electromagnetic spectrum (Schaber et al., 1976; Daily et al., 1978a,b,c).

The launch and successful operation of the L-band SAR on Seasat was a major step in demonstrating the capability of synoptic and large areal mapping using spaceborne SARs. Preliminary analysis of the Seasat-A SAR image indicates the potential for this to be a major remote sensing tool which would complement Landsat for the monitoring and assessment of Earth resources.

The cloud penetration capability of the SAR makes this sensor the only tool that can be used to map the surface of Venus. NASA is presently planning a VOIR (Venus Orbiting Imaging Radar) mission to provide global mapping of the Venusian surface with a resolution of a few hundred meters, with limited targetable mapping capability at a higher resolution (~50 meters).

In order to be able to define the desirable characteristics of the VOIR radar, such as frequency, polarization and viewing geometry, research is ongoing to understand the radar signature of a number of geologic terrains which might be encountered on Venus.

In this paper, we report on some aspects of our activities as related to the study of volcanic fields and sand fields using airborne and Seasat SAR data. The different remote sensing systems used in this study are described in Table 1. The locations of the sites under study are indicated in Figure 1. In Section II we give a brief overview of radar backscatter theories which are directly relevant to this work. In Section III we discuss the radar, photographic and ground observations of the different volcanic fields under study and provide an explanation of the radar signature observed. Section IV will address the different sand dune fields studied. Section V summarizes our results and provides recommendations for future research.

II. OVERVIEW OF RADAR SCATTERING THEORIES AS APPLIED TO GEOLOGIC SURFACES

In order to interpret radar images, the geologist used two different types of information: (a) geometric patterns such as lineaments, texture, contacts, shapes, etc., in a way similar to what is done in the interpretation of visible and IR photography, and (b) the radar backscatter (or image tone) of specific features to derive information on the macrorelief (such as slope) and subresolution microrelief (roughness) structure of the surface.

The radar backscatter from geologic surfaces (scattering from vegetated surfaces is not discussed here) is dependent on the following surface parameters: (a) surface slope, (b) surface roughness at the scale of the wavelength, (c) dielectric constant of surface material, and (d) subsurface inhomogeneities, particularly in very dry regions.

For surfaces where there are plane smooth facets which are many radar wavelengths in dimension (such as slip faces of dunes or blocky lava), quasispecular backscatter is usually dominant. In this case, most of the backscattered radar energy comes from facets which are oriented perpendicular to the incident wave vector. This type of backscatter is usually relatively strong becuase all of the energy is conserved in the reflected and transmitted directions (very little scattered in other directions). This type of scattering is usually encountered while imaging at small incidence angles (of up to about 30 degrees from the vertical). However in the case of block lava flows, specular return can occur at even higher incidence angles because lava block facets can be encountered at nearly all angles. Another important factor is that single and double specular backscattering does not depolarize electromagnetic waves. Thus, this type of scattering is important in the interpretation of like-polarized images. Also, it should be pointed out that specular scattering is not dependent upon the radar frequency as long as the surface is smooth relative to the observing radar wavelength.

Table 1. Remote sensing systems

Type[a]	Band	Polarizations	Wavelength (cm)	Organization	Resolution (m)	Altitude (km)	Incidence Angle	h (cm)
RAR	K	HH, HV	0.86	Westinghouse Aerospace	15	Not Available	65°	0.2
SAR	X	HH	3	Goodyear Aerospace	12 3 (Amboy)	10	65°	0.8
SAR	L	HH, HV	25	JPL	25	10	40°	4
Sea-sat-A	L	HH	23.5	JPL/NASA	30	800	20°	3.2

[a] RAR - Real Aperture Radar;

SAR - Synthetic Aperture Radar.

[b] Incidence angle = 90 - depression angle.

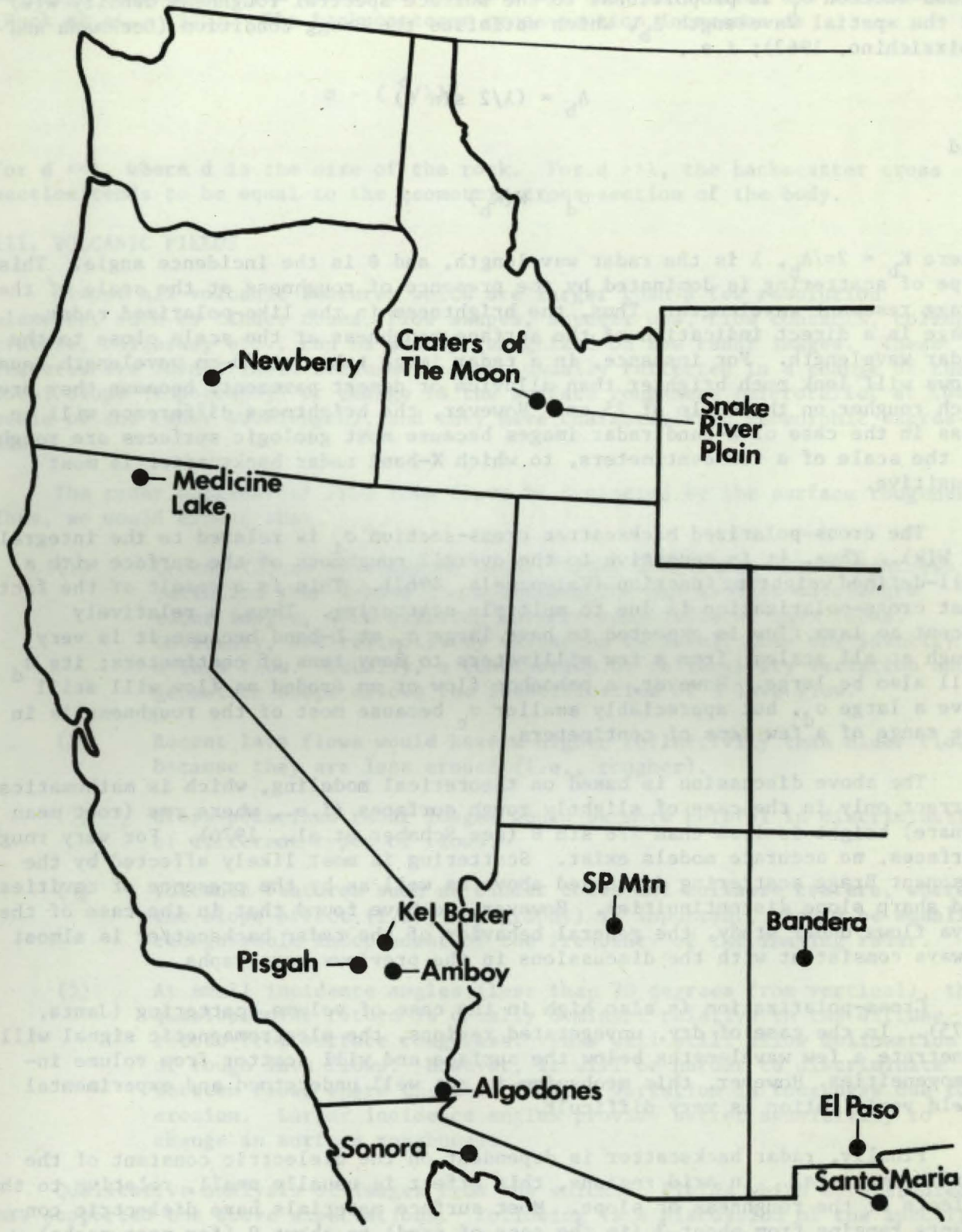

Figure 1. Map of western United States showing locations of study areas.

In the case of slightly rough surfaces, the like-polarized backscatter cross-section σ_L is proportional to the surface spectral roughness density W(k) at the spatial wavelength Λ_b, which satisfies the Bragg condition (Beckmann and Spizzichino, 1963); i.e.,

$$\Lambda_b = (\lambda/2 \sin \theta)$$

and

$$\sigma_d \sim W(K_b)$$

where $K_b = 2\pi/\Lambda_b$, λ is the radar wavelength, and θ is the incidence angle. This type of scattering is dominated by the presence of roughness at the scale of the Bragg resonant wavelength. Thus, the brightness in the like-polarized radar image is a direct indication of the surface roughness at the scale close to the radar wavelength. For instance, in a radar image taken at 25-cm wavelength lava flows will look much brighter than alluvium or desert pavement, because they are much rougher on the scale of 25 cm. However, the brightness difference will be less in the case of X-band radar images because most geologic surfaces are rough at the scale of a few centimeters, to which X-band radar backscatter is most sensitive.

The cross-polarized backscatter cross-section σ_i is related to the integral of W(k). Thus, it is sensitive to the overall roughness of the surface with a well-defined weighting function (Valenzuela, 1967). This is a result of the fact that cross-polarization is due to multiple scattering. Thus, a relatively recent aa lava flow is expected to have large σ_i at L-band because it is very rough at all scales, from a few millimeters to many tens of centimeters; its σ_d will also be large. However, a pahoehoe flow or an eroded aa flow will still have a large σ_d, but appreciably smaller σ_c because most of the roughness is in the range of a few tens of centimeters.

The above discussion is based on theoretical modeling, which is mathematically correct only in the case of slightly rough surfaces (i.e., where rms (root mean square) height is less than $\lambda/8 \sin \theta$ (see Schaber et al., 1976). For very rough surfaces, no accurate models exist. Scattering is most likely affected by the resonant Bragg scattering discussed above as well as by the presence of cavities and sharp slope discontinuities. However, we have found that in the case of the lava flows under study, the general behavior of the radar backscatter is almost always consistent with the discussions in the previous paragraphs.

Cross-polarization is also high in the case of volume scattering (Janza, 1975). In the case of dry, unvegetated regions, the electromagnetic signal will penetrate a few wavelengths below the surface and will scatter from volume inhomogeneities. However, this mechanism is not well understood and experimental field verification is very difficult.

Finally, radar backscatter is dependent on the dielectric constant of the surface material. In arid regions, this effect is usually small, relative to the effects of the roughness or slope. Most surface materials have dielectric constants ranging from about 3 (in the case of sand) to about 9 (for most rocks). This variation leads to a variation in the power reflection coefficient of about 2 (i.e., 3 dB). In comparison, backscatter variations of more than 10 dB are commonly encountered due to roughness or slope variations.

Another type of scattering which sometimes plays an important role is the Rayleigh scattering from bodies of finite shape such as pebbles and rocks (Ruck et al., 1970). The backscatterer cross-section increases as

$$\sigma \sim (d/\lambda)^4$$

for $d \ll \lambda$, where d is the size of the rock. For $d \gg \lambda$, the backscatter cross section tends to be equal to the geometric cross-section of the body.

III. VOLCANIC FIELDS

Almost all volcanic features which are larger than a few resolution elements, such as cinder cones, flow shapes, squeeze ups, flow contacts, collapse craters, calderas, etc., can be easily recognized on the radar images. These features are identifiable because they are usually reflected in a change of the local slope (topography) or change in the surface roughness (microrelief at the scale of the radar wavelength), and they have characteristic geomorphic expressions.

The radar backscatter from lava flows is dominated by the surface roughness. Thus, we would expect that

(1) L-band (25-cm wavelength) radar images would show more brightness variation than X-band (3-cm wavelength) and shorter wavelength radar images, thus allowing better recognition of lava flows. Obviously, the reflectivity variation by itself does not identify a lava flow. Usually, a combination of reflectivity variation and geometric shape allows the identification of a lava flow.

(2) Recent lava flows would have a higher reflectivity than older flows because they are less eroded (i.e., rougher).

(3) Cross-polarized radar images would be more helpful in discrimination of different types of flows.

(4) Volcanic features such as cinder cones and collapse craters, where the slope effect (i.e., topography) is important, should be equally recognizable independent of the frequency of the imaging radar.

(5) At small incidence angles (less than 30 degrees from vertical), the quasispecular return is usually dominant relative to the diffuse return from surface roughness. This will still allow delineation of rough lava flows. However, it will be harder to discriminate between flows where there is limited variation in roughness due to erosion. Larger incidence angles provide better sensitivity to change in surface roughness.

Qualitative analysis of images from the volcanic fields which were studied has supported the above expectations. Following is a discussion of the specific sites studied. The results of the studies on SP lava flow (Arizona) and Askja Caldera flow in Iceland have been reported elsewhere (Schaber et al., 1979; Malin et al., 1978; Evans, 1978).

IV. OBSERVATIONS

A. Pisgah Crater and Lava Field

Pisgah Crater and lava field are located about 60 km east of Barstow in the Mojave Desert of California (Figure 1). The lava field is about 23 km long, more than 6 km wide, and has an area of 80 km^2. Pisgah Crater is a cinder cone nearly 100 m high and 488 m in diameter at the base. Lavic lake, a playa about 3.5 km in diameter, lies at the southeast end of the lava field.

Pisgah lava field formed in three eruptive phases which were distinguished on the basis of phenocryst textures (Wise, 1966). Each phase resulted in the formation of a cinder cone. The first two cones are nearly eroded away and the most recent is presently being mined for cinders. The first-and second-phase flows were more voluminous than the third. The first flow is pahoehoe, now broken up. The second flow is predominantly aa and the third is pahoehoe with numerous pressure ridges, lava tubes, and tumuli. Wind-blown material has accumulated in pockets on the pahoehoe surfaces. Figure 2a is a geologic map of Pisgah lava field from Wise (1966).

Pisgah lava field was imaged by all the sensors listed in Table 1 (Figures 2, 3, and 4). The dominantly pahoehoe units (first and third eruptive units) and the aa lava of the second phase of eruption are distinguishable on LHV (L-band, horizontal transmit, vertical receive) and KHV radar images. The aa-pahoehoe contact can barely be discerned in the LHH image and cannot be seen in the XHH and KHV images. The first and third flow units cannot be separated on any of the images. In LHV, the second unit is brighter than its surroundings. This effect was suggested by Sabins (1978, p. 399), and is similar to the effect noted for SP lava flow by Schaber et al. (1979). In the KHV image, the aa flows are darker than the surrounding pahoehoe, while in the KHH image, the lava field has a uniform reflectivity. Dellwig and Moore (1966) and Mc Cauley (1972) explained high KHH returns from blocky surfaces by single reflection from properly oriented block facets. Thus, the aa of the second phase appears to be blocky at K-band (0.86-cm wavelength) and rough at L-band (25-cm wavelength). The second unit can also be separated from the first and third units in the Landsat image (Figure 4a). The second unit is darker at visible and near infrared wavelengths partly because of shadowing in the rough aa lavas.

Discrimination between aa and pahoehoe lavas is also possible in the Seasat-A (LHH) image (Figure 4b). The aa areas to the east and southeast of Pisgah Crater are slightly brighter than the surrounding pahoehoe, as in the LHH image acquired by aircraft (Figure 3c). An area of hummocky pahoehoe west of Pisgah Crater is also bright in the Seasat-A image. This is probably caused by the low slope angles of the hummocks furnishing normal specular reflection at the small incidence angle of Seasat-A (20°) and not at the larger incidence angles characteristic of the aircraft images.

The sand-covered western tongue of pahoehoe is difficult to separate from its surroundings in K-band images, but X- and L-band clearly show the flow boundaries. This implies either that only the smallest scale (<1 cm) surface roughness has been masked by the wind-blown sediment or that longer wavelengths are able to penetrate the sediments. Aeolian material visibly masks portions of the flow in the Landsat image (Figure 4a).

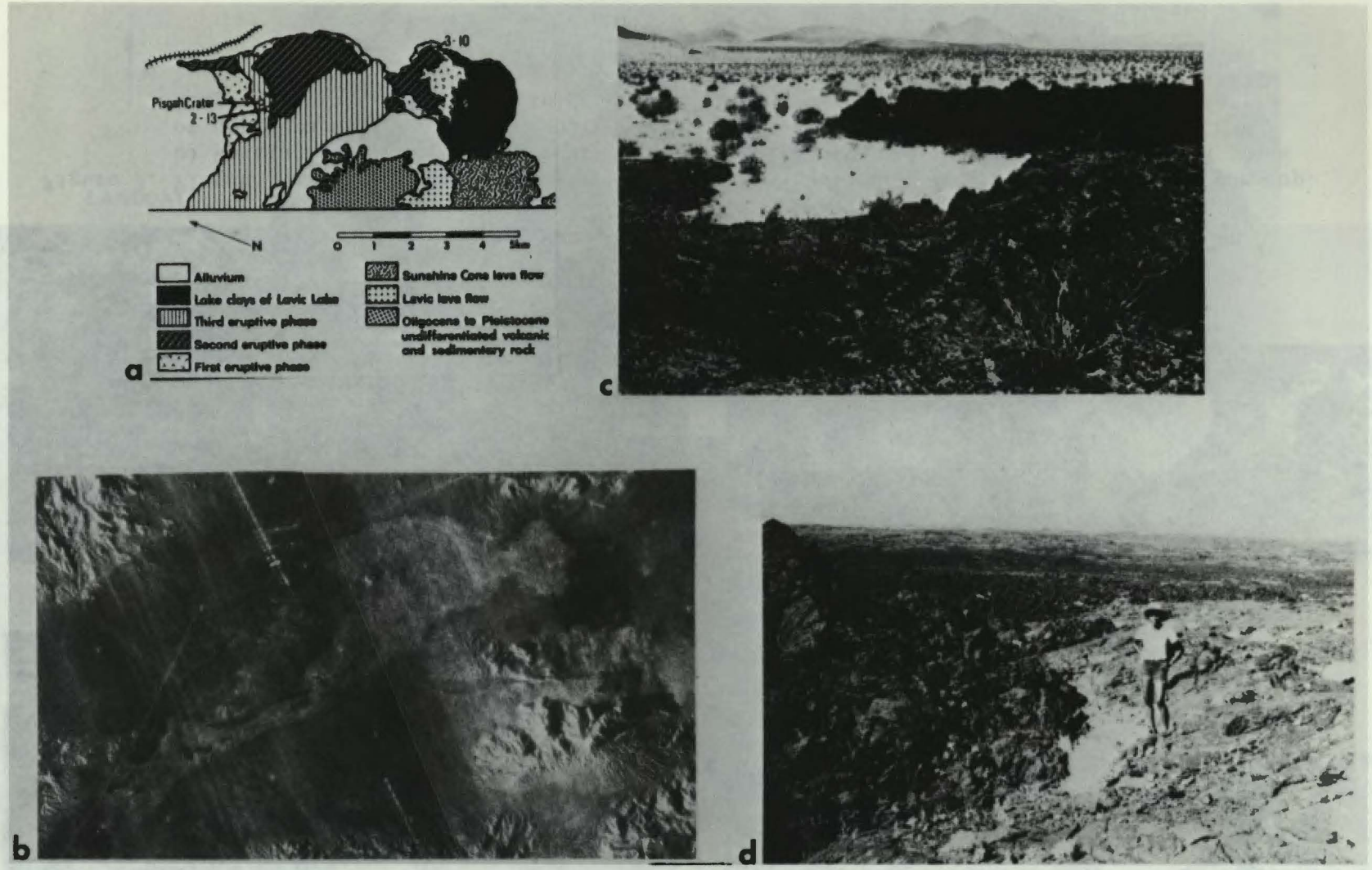

Figure 2. Pisgah lava field. a) Geologic map modified from Wise (1966). b) Goodyear XHH image acquired before 1970. Illumination is from lower left. Orientation and scale is the same as in a). c) Contact of phase one lava with alluvium. Flow front is 2-3 m high. The surface is broken up pahoehoe. Ground photo 3-10, located shown in a). d) Contact between second phase aa (left) and third phase pahoehoe (right). Ground photo 2-13, location shown in a).

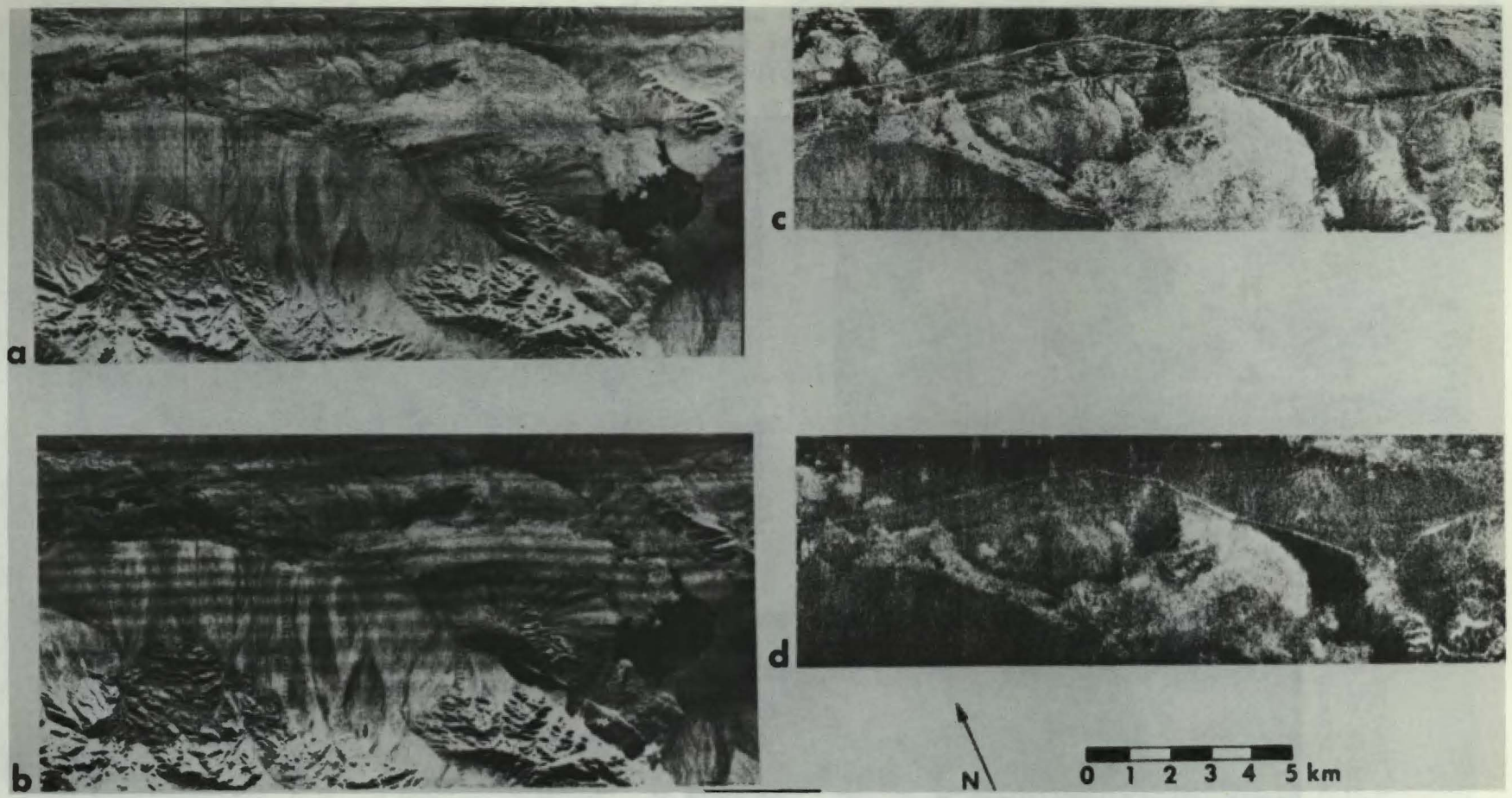

Figure 3. Pisgah lava field. a) Westinghouse KHH image acquired in 1965. Illumination from top. b) Westinghouse KHV image acquired in 1965. Illumination from top. c) JPL LHH image of northern half of field acquired 3 May 1978. Illumination from top. d) JPL LHV image of northern half of field acquired in May 1978. Illumination from top.

Figure 4. Pisgah and Amboy lava fields. a) Part of Landsat frame 5474-17002, band 7 showing Pisgah lava field (left) and Amboy lava field (lower right). Acquired 5 August 1976. b) Digitally correlated Seasat-A SAR image covering same area as a). Illumination from lower left. Revolution 882, 27 Aug. 1978.

The cinder cone of Pisgah Crater is clearly delineated on the K- and X-band images because of their small depression angles and the resulting shadows, and on the Seasat-A image because, at the small incidence angle, surface slope change leads to a large tonal change in the image. It is barely discernible on the aircraft L-band image.

B. Amboy Crater and Lava Field

Amboy Crater and lava field are located 130 km east of Barstow in the Mojave Desert of California (Figure 1). The lava field is nearly circular, about 10 km in diameter, and has an area of about 70 km^2. Amboy Crater is an undissected, composite cinder cone 75 m in height and about 460 m in diameter at its base. The lava field is mostly composed of undifferentiated flows of degassed pahoehoe that form a hummocky terrain. Surface relief ranges from 2 to 5 m. The oldest flows are platform units that contain collapse depressions up to 10 m in diameter and several meters deep. Younger platform units are isolated areas of uniform, relatively flat basalt that were probably not disturbed while cooling. Vent lavas are exposed at the presumed location of a main vent for the lava field. They form plateaus of relatively dense pahoehoe about 10 m high. The vent plateaus have some collapse depressions and are generally ringed by fractures (Figures 5a, b), indicating subsidence either by draining back into the vents or through production of secondary flows. In addition to the collapsed features, there are several piles of boulders 1 to 4 m high that have been interpreted to be explosive features (Parker, 1963; Greeley and Iversen, 1978). Most low lying areas and hollows in the lava field are filled with aeolian deposits as much as 1 m thick. A few prominent sediment-free streaks trail downwind from such topographic features as the cinder cone and vent plateaus.

XHH, LHH, LHV and Seasat-A radar data were available for Amboy Crater and lava field (Table 1, Figures 4b and 6). The X-band image has sufficient resolution for recognition of many geomorphic types within the flow. The vent lavas and some of the remnant platform units that have relatively smooth desert pavement surfaces are prominent. The undifferentiated flows are very irregular, as the many shadows and bright radar returns indicate. Amboy Crater can be seen in the images because the large incidence angle of the X-band system accentuates topographic features.

The large subsidence fractures around the peripheries of the vent areas are visible in the X-band image as dark lines, because aeolian material has filled the fractures leaving smooth floor. The collapse depressions stand out as circular areas with dark centers for the same reason. The chaotic piles of boulders on the main vent plateau are visible as bright point returns.

Although the L-band images have a lower resolution than the X-band image, the vent lavas and remnant platform units are visible. Subsidence features and the chaotic piles of boulders are not visible on the L-band images because of their lower resolution. The morphology of Amboy Crater is reasonably well delineated, though shadowing is decreased because of the lower incidence angle of the L-band systems. Image layover is particularly noticeable in the Seasat-A images and Landsat image. The oldest platform unit on the east side of the flow, however, is not obvious on any of the images and appears to be buried by the alluvial material of Bristol Lake.

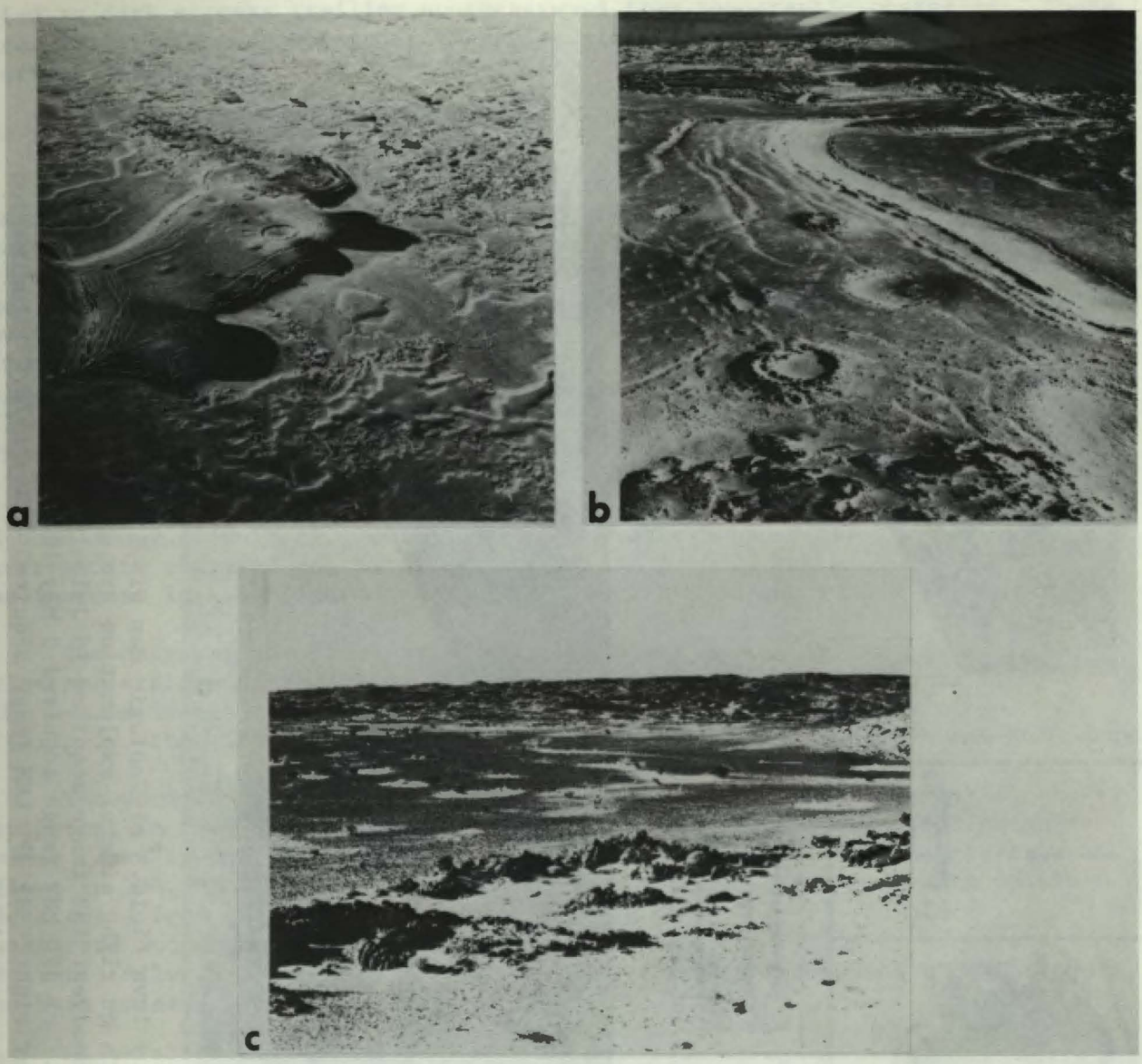

Figure 5. Amboy lava field. a) Aerial view south of vent plateau near center of lava field. Lava knobs and subsidence features visible on the plateau. The irregular surface of the rest of Amboy lava field is also visible. Photo by J. Iversen from Greeley and Iversen from Greeley and Iversen (1978). b) Aerial view northeast of vent plateau in a). Aeolian material partly fills subsidence features. Photo by R. Greeley. c) Ground photo of remnant platform unit on northeast side of Amboy Crater. Area has smooth desert pavement surface.

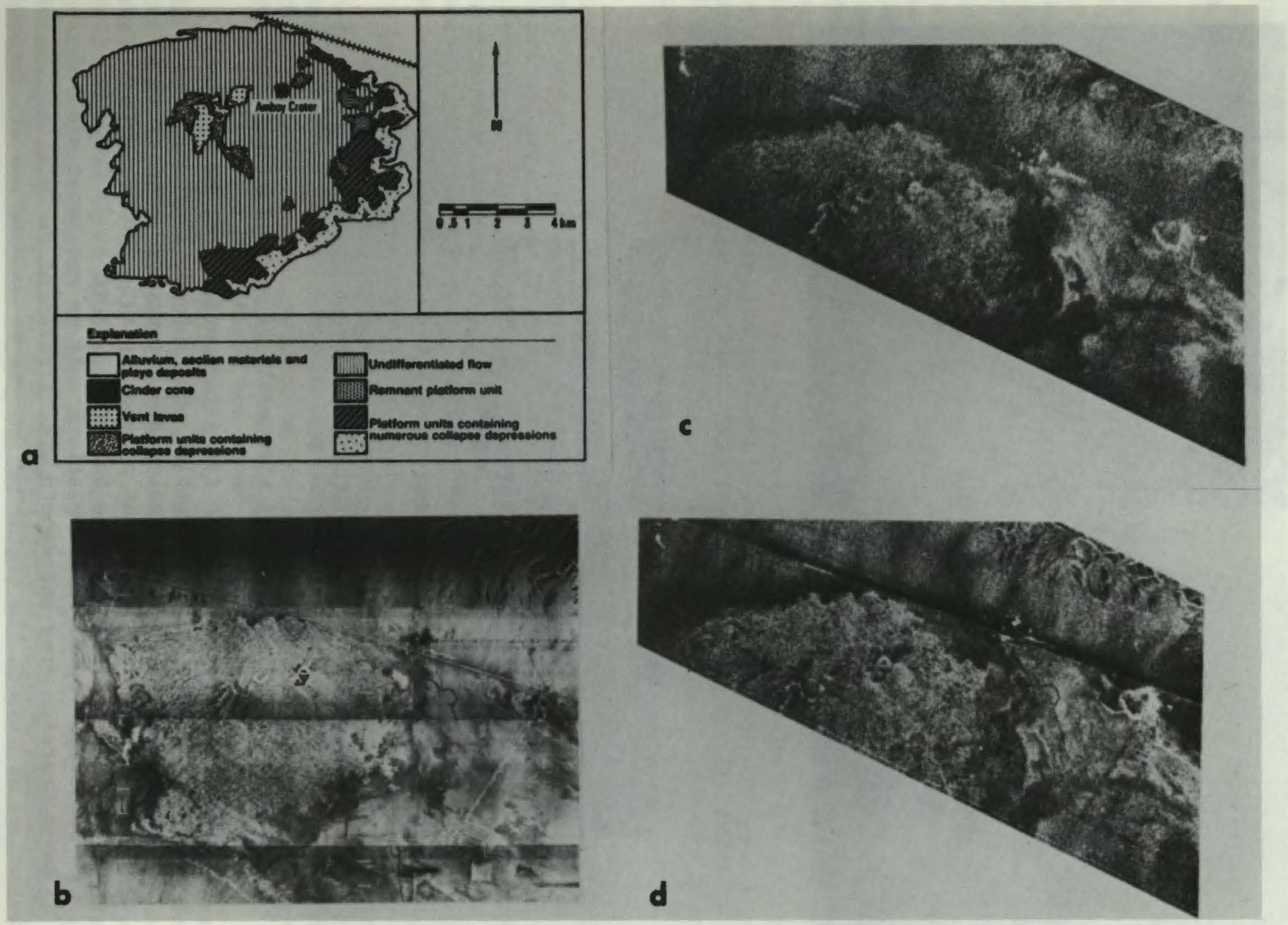

Figure 6. Amboy lava field. a) Geologic map simplified from Hatheway (1971). Units on right side of explanation are older than units on left. b) Goodyear XHH image acquired 19 Jul. 1976. Illumination from top. c) JPL LHV image acquired 3 May 1978. Illumination from upper right. d) JPL LHH image acquired 3 May 1978. Illumination from upper right.

The aeolian material masking portions of Amboy lava field is clearly shown in the Landsat image by the lighter tone of the lava field as compared to Pisgah lava field (Figure 4a). The sediment-free wind shadows are also easily identified as dark streaks trailing southeastward from topographic obstacles. These areas are visible on the radar images as slightly brighter returns because the surface roughness is less attenuated.

C. Kel-Baker Volcanic Field

The Kel-Baker Volcanic Field is an area of some two dozen cinder cones and associated basaltic lava flows about 145 km east of Barstow, between Kelso and Baker in the Mojave Desert of California (Figure 1). The flows are as much as 15 m thick and cover an area of more than 75 km^2. Most of the flows rest upon a pediment formed on the Cretaceous Teutonia quartz monzonite. Elsewhere the flows overlie alluvium or Precambrian gneiss. The flows and cinder cones range in age from Pliocene to Recent, some possibly as young as a few thousand years. The older flows are weathered, eroded, and partially vegetated. The most recent flows and cinder cones preserve a rough hummocky aa lava surface. No soil or vegetation has been established on these flows (Figure 7) (Barca, 1965).

The flows are much more easily separated on the L-band images than on the X-band image (Figure 8). Reflectivity contrasts between the flows and their surrounding alluvium are larger at L-band and nonexistent at X-band. There is an increase in LHH brightness with decreasing age of the flows.

The only way the flows can be distinguished in the X-band image is by specular reflection and shadowing at their flow fronts. This effect is also seen in the L-band images as most of the field was imaged at a large incidence angle. Similarly, the cinder cones of the field show up well in both LHH and XHH image.

The youngest flow in the southern part of the field (Figure 7b) is the brightest in the L-band images. It is much brighter than the alluvium and the older flows in LHV, whereas it is only slightly brighter than the other lava flows in LHH. The high cross-polarized return is probably caused by multiple scattering from the very rough surface of the young flow. The older flows are weathered and eroded (Figure 7d), providing a relatively low cross-polarized return. Alluvium and desert pavement areas are very smooth and therefore dark on both polarizations.

D. Medicine Lake Highland

Medicine Lake Highland is about 55 km east of Mount Shasta and south of Lava Beds National Monument in northern California (Figure 1.) The highland begins at an elevation of about 1500 m and rises to an elevation of almost 2400 m. It has an area of about 50 km^2 and a basal diameter of 35 km. It is surrounded by an elliptical rampart of cinder cones and domes, the highest of which is Mount Hoffman, at 2418 m. The highland is forested, except on the most recent lava flows. Medicine Lake Highland is the remnant of a shield volcano on the east boundary of the Cascade Range. The central portion collapsed to form a caldera, and ring fractures around the periphery of the caldera became the sites of eruptions of viscous andesitic lavas, which built the rampart of cones that enclose the caldera. In most recent times, dacites, rhyodacites, and rhyolites erupted on the rampart and on the floor of the caldera. At about the same time, basalt flows erupted on the flanks of the volcano. The flows of Lava Beds National

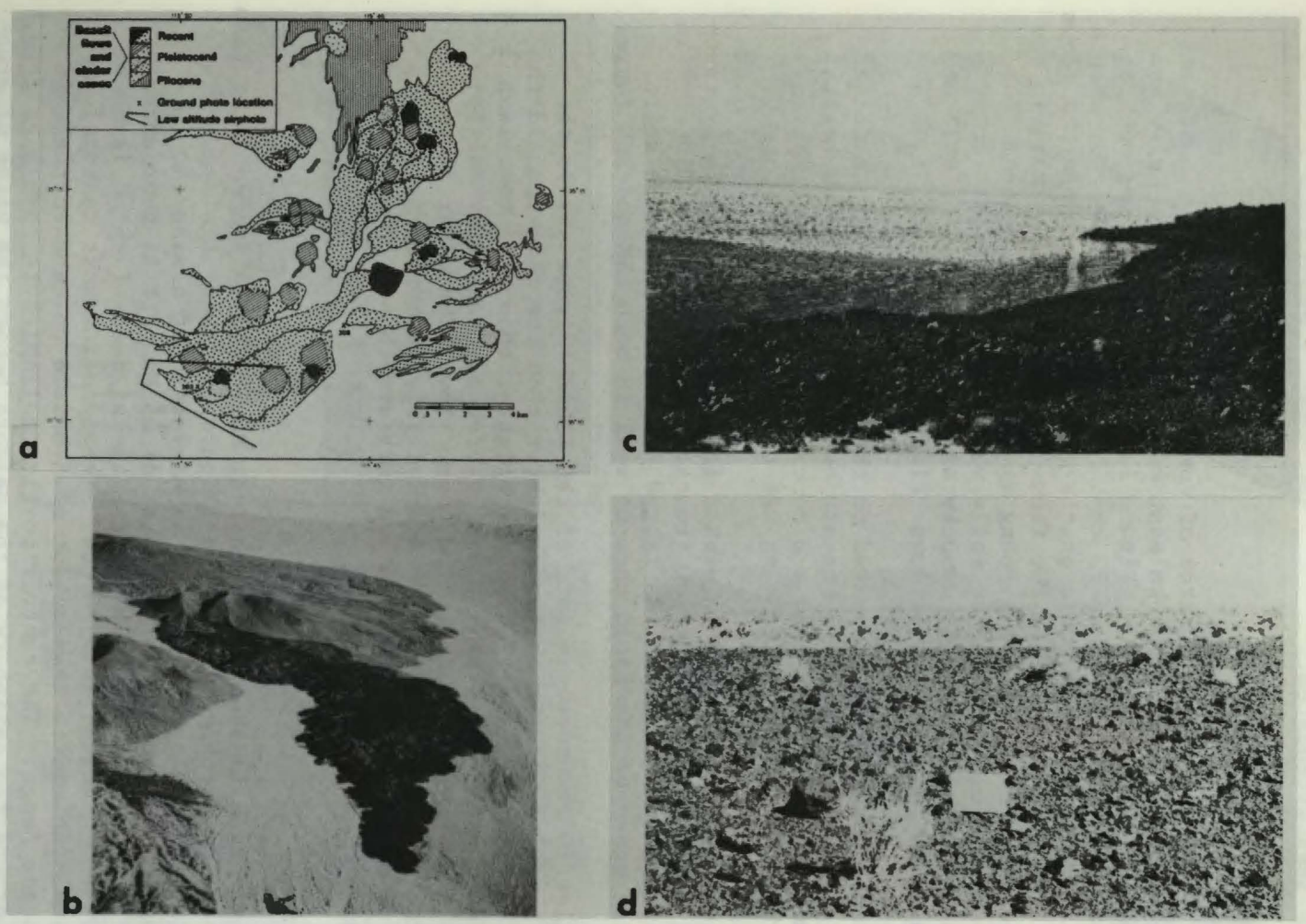

Figure 7. Kel-Baker volcanic field. a) Preliminary geologic map by W. Wise (unpublished; written communication, 1978). b) Low altitude air photo of the youngest flow, in the southwest corner of the field. View east photo by R. Greeley. c) Ground photo showing rough aa surface of youngest flow in foreground, dark desert pavement surface derived from older flow in middle ground, and light colored vegetated alluvial surface beyond. Photo number 303. d) Surface of older flow to northeast of youngest flow. Surface is sparesely vegetated cobble pavement. Chalkboard is 20 cm square. Photo number 308.

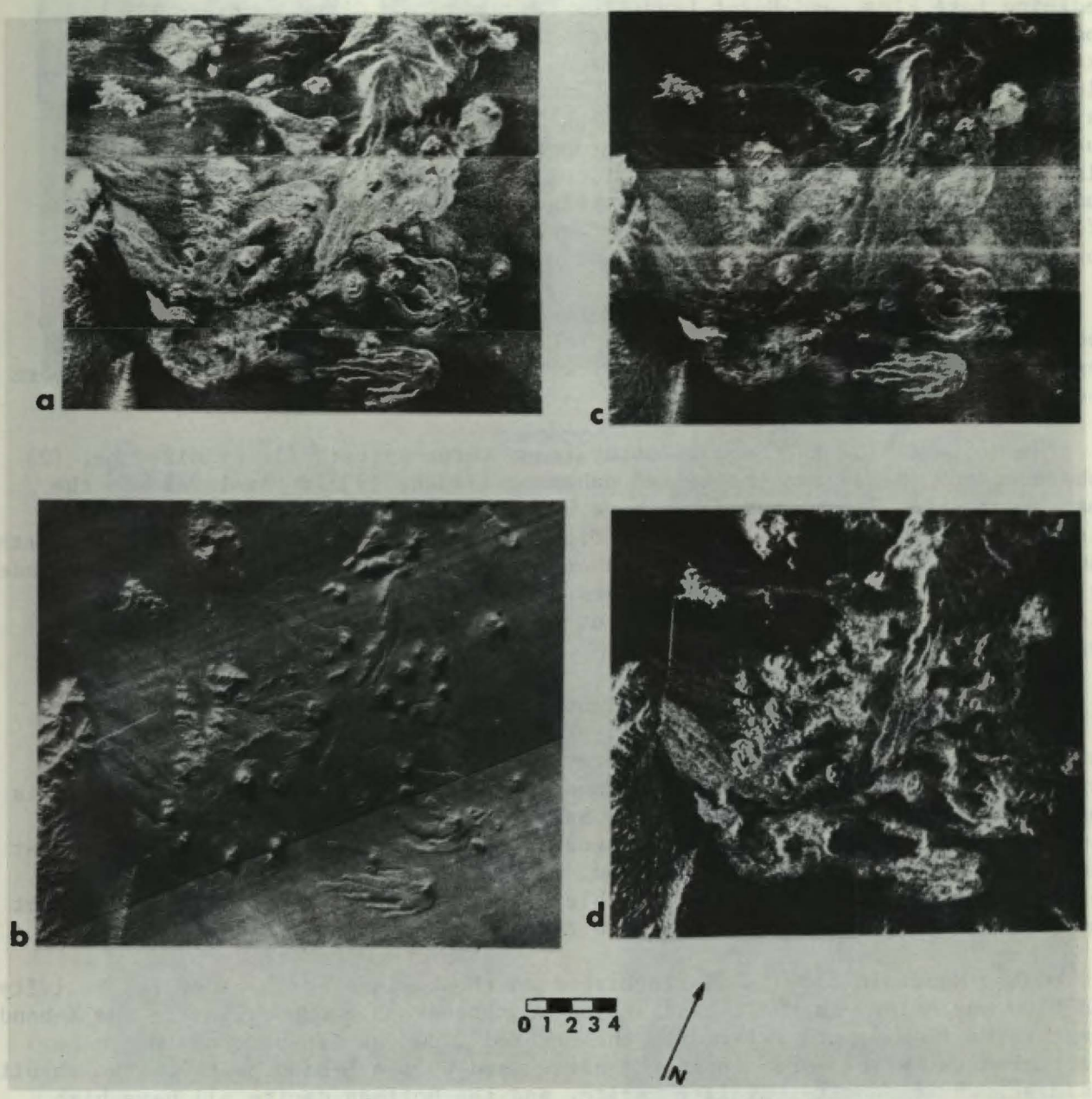

Figure 8. Kel-Baker volcanic field. a) JPL LHH mosaic obtained 30 Aug. 1977. Illumination from top. b) Goodyear XHH image acquired before 1970. Illumination from upper left. c) JPL LHV mosaic obtained 30 Aug. 1977. Illumination from top. d) Optically correlated Seasat-A SAR image acquired 14 Sept. 1978 (Rev. 1140). Illumination from left.

Monument to the north and Burnt Lava Flow to the south are examples of these parasitic flows. Numerous cinder cones also formed at this time (Anderson, 1941).

Three of the Recent flows were studied in detail: Glass Mountain Flow, Medicine Lake Flow, and Burnt Lava Flow (Figure 9d). Glass Mountain Flow is a composite flow including an early phase of explosive cone building followed by extrusion of stony dacite and rhyolite obsidian. The western extension of the flow partially covered the earlier Hoffman dacite. Most of the composite flow is rhyolite obsidian with a pumiceous surface and glassy interior. A second, much smaller rhyolite obsidian flow erupted later and formed high flow fronts distinct from the earlier composite flow. The surface of this flow is also pumiceous to scoriaceous. The final stage of activity was marked by the rise of a dome of rhyolitic glass, the surface of which is partly pumiceous and covered with glassy spines (Anderson, 1941).

Medicine Lake Flow is a small dacite flow (about 2.5 km^2 in area) north of Medicine Lake. The flow has high (15 to 45 m) lobate flow fronts and an irregular, blocky surface (Figure 10b,c) with enough ash-filled pockets to support a sparse tree growth.

Burnt Lava Flow is composed of at least three units: (1) oxidized aa, (2) pahoehoe, and (3) aa and fragmented pahoehoe (Finch, 1933). Aa lavas are the most prevalent. Two main sources have been found for Burnt Lava Flow: the cinder cone called High Hole Crater (Figure 9d) and a linear fissure on the north end of the flow (Anderson, 1941). Several older cinder cones have been surrounded by Burnt Lava Flow. These cinder cones are more eroded and forested than High Hole Crater. The surface of Burnt Lava Flow is practically devoid of vegetation (Figure 10a).

Burnt Lava Flow shows up as a light tone in all the radar images because of its rough, unvegetated aa surface. The contrast between the flow and the surrounding coniferous forest is greater at L-band than at X-band. A probable explanation for this contrast difference is that the top of the forest canopy is rougher to X-band and scatters nearly as much energy as the lava flow. Forest clear cuts, visible on the L-band images as dark areas, indicate that the forest has a reasonably high return at L-band, but not as high as the return from the aa flow. The clear cuts are not visible on the X-band image; however, it is not known whether they existed at the time the X-band data were obtained.

Glass Mountain Flow is distinguished on the basis of high radar reflectivity and flow morphology on the L-band images and topographic expression in the X-band image. The flow fronts related to the several flows at Glass Mountain can be discriminated by the large incidence angle used by the X-band system. The rhyolite obsidian, the composite rhyolite-dacite, and the Hoffman dacite all have high (~30 m) flow fronts. In addition, the Hoffman dacite has a concentric flow-ridge structure visible on the X-band image. The rhyolite obsidian flow front is also visible on the L-band images. No reflectivity differences are apparent between the flows in the X-band image. The Hoffman dacite, however, is distinguishable from the glass flow in both L-band images because of the different tone: ash and forest cover on this flow appear to affect L-band more than X-band.

The high flow fronts of Medicine Lake Flow are visible in both X- and L-band images. The flow is at a larger incidence angle than Glass Mountain on the L-band images, and topographic effects are therefore much greater. Reflectivity of the flow at X-band is only slightly greater than the surrounding forest. The flow is clearly delineated by the shadow of the flow front in the far range. In the LHH

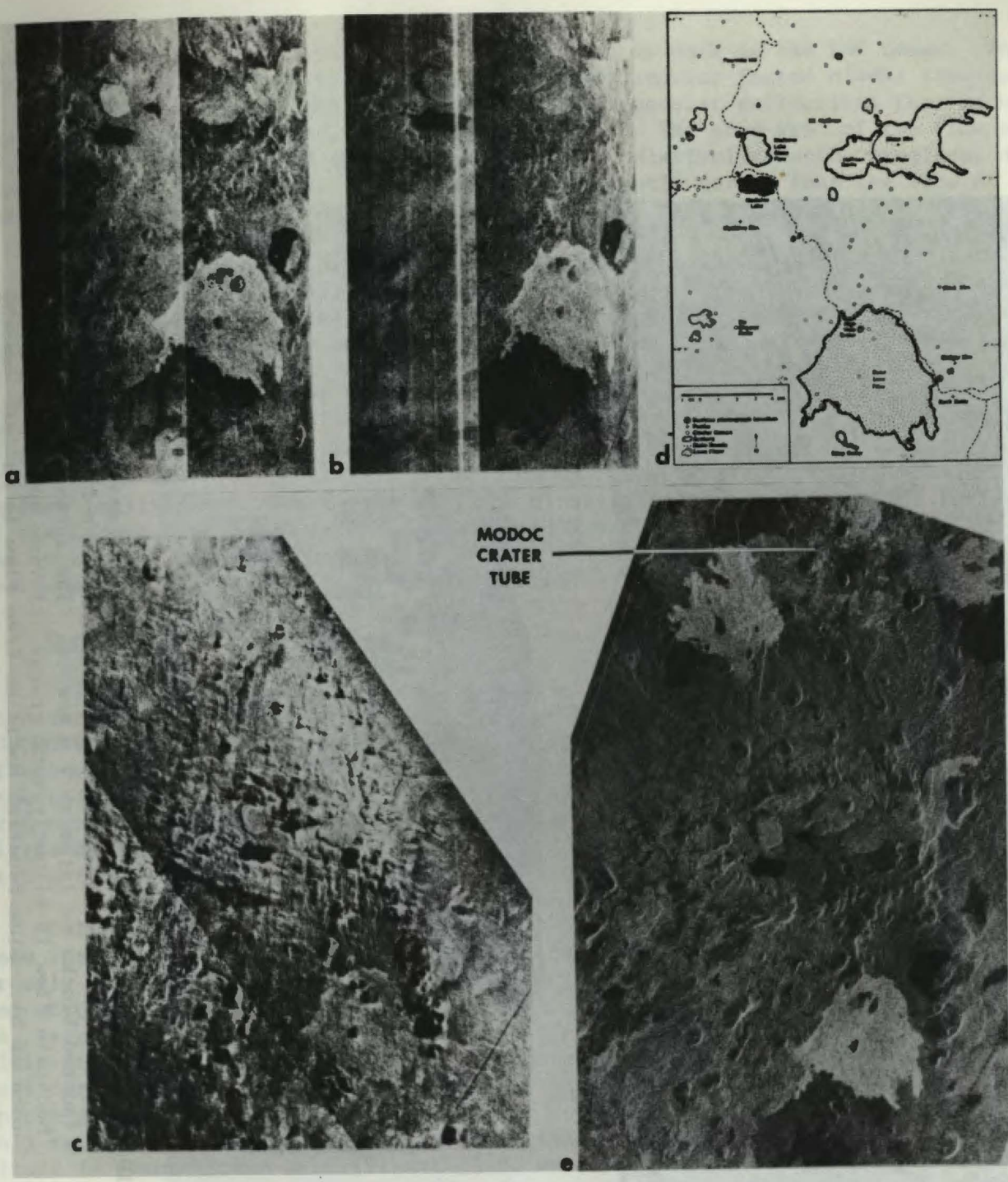

Figure 9. Medicine Lake Highland. a) JPL LHH image acquired 6 Sept. 1977. Dark checkerboard south of and dark area northeast of Burnt Lava Flow are clear cuts. Illumination from right. b) JPL LHV image acquired 6 Sept. 1977. Illumination from right. c) Goodyear XHH image acquired before 1979. Illumination from upper right, d) Location map showing major lava flows and cinder cones. e) Digitally correlated Seasat-A SAR image acquired 3 Oct. 1978. (Ref. 1406). Area shown is larger than a, b,c, and d. Bright areas at top are flows in Lava Beds National Monument. Modoc Crater Lava Tube is indicated.

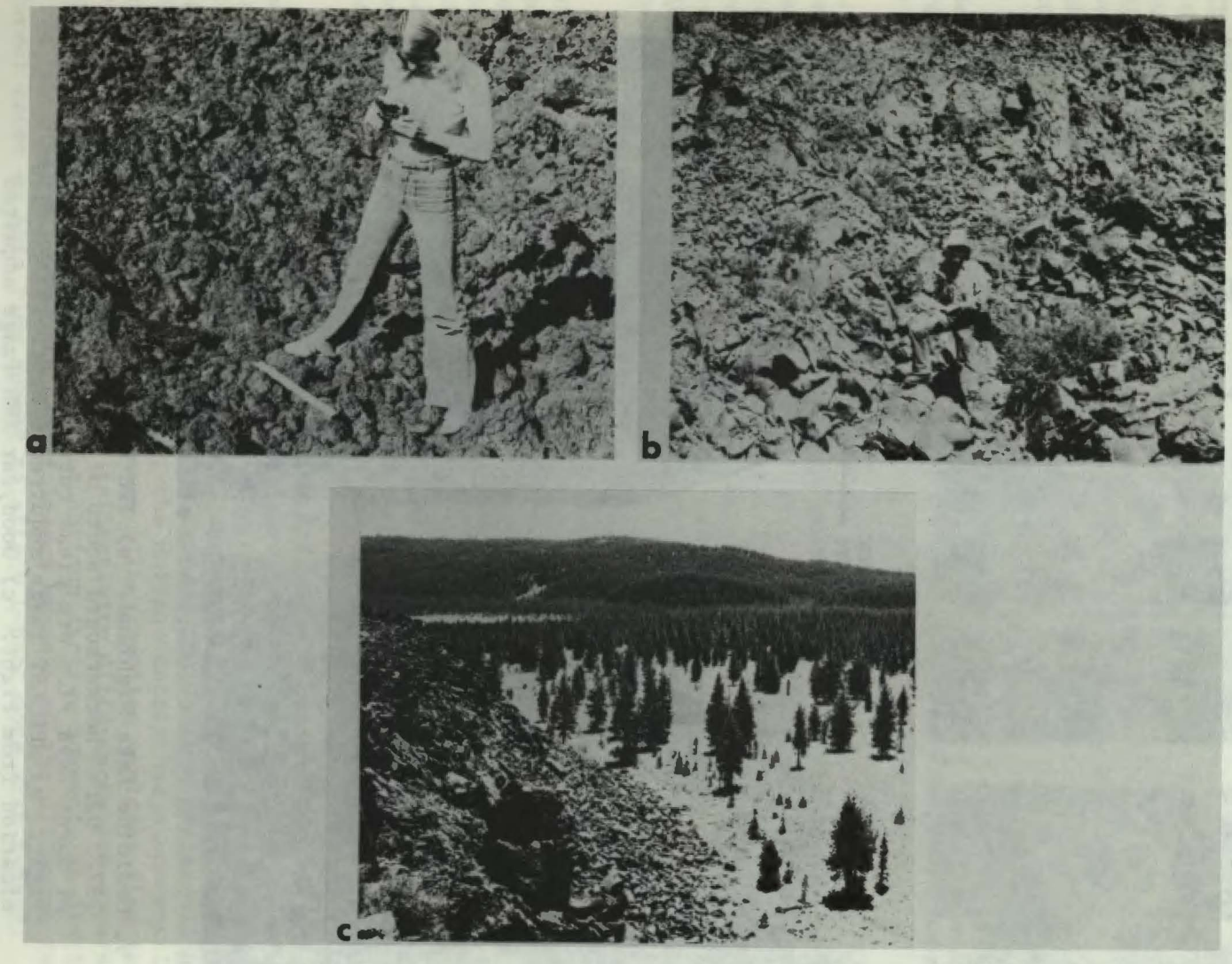

Figure 10. Medicine Lake Highland. a) Surface of Burnt Lava Flow. Note craggy, jumbled texture. b) Surface of Medicine Lake Flow. Note faceted blocks as large as 2 m across. The surface of glass Mountain Flow is slightly more craggy. c) View south from location of b). Flow front of Medicine Lake Flow is on left smooth, ash covered plain on right. Medicine Lake is in left background.

image, the entire flow is very bright, whereas it is dark in the LHV image. This effect could be explained by the large, extremely angular facted blocks that make up this surface (Figure 10b). These blocks give specular reflections that do not depolarize the radar signal, as discussed earlier. The area west of the flow edge, that is dark on the L-band images, consists of a relatively smooth, treeless, ash-covered plain (Figure 10c). The area is only slightly darker than the flow on the X-band image.

Other geomorphic features of interest in the Medicine Lake Highland include cinder cones and lava tubes. Cinder cones are easily visible on the X-band image. Its high resolution and small depression angle emphasize topographic features. Some details are hidden in shadow, but the morphology of cones and summit craters is usually well presented. High Hole Crater on Burnt Lava Flow is a good example. Cinder cones can be seen in the aircraft L-band images, but their morphology is more difficult to interpret because lower resolution and small incidence angles produce few shadows. However, in the extreme case of the Seasat-A radar, the cinder cones are clearly visible because of near specular return from the cones' surface inclined toward the radar. A few cinder cones appear in the far range of the L-band images and sections of several lava tubes have been identified. The lava tubes appear as bright curvilinear features, probably caused by collapsed sections of roof. Modoc Crater Tube (Hatheway, 1971) is indicated in Figure 9e.

E. Eastern Snake River Plain

Volcanic rocks of the eastern Snake River Plain lie in a northeast-trending structural depression in southeastern Idaho (Figure 1). Most of the approximately 30,000 km^2 of the eastern plain is covered by Quaternary basalt and lesser amounts of alluvial sand and gravel. Russell (1902) described the eastern plain as constructed by vast floods of extremely fluid basalt that poured in all directions from many local vents, thus building a broad, nearly level plain, still relatively little dissected. Igneous rock types in the area are dominantly olivine tholeiites with a few plugs of more silicic rock.

Only dual polarization L-band (LHH and LHV) and Seasat-A images were available for the Snake River Plain. Radar returns from its volcanic units can be broadly classified as weak from Pleistocene lavas (Qb_4, Qb_3 and Qb_2 in Figure 11d) and strong but more variable from Recent flows (Qb_1). Volcanic units older than Qb_1 return very little radar energy because of their smooth surfaces. The Pleistocene volcanic units (Qb_{2-4}) are covered by loess and, in some places, by soil derived from weathering of the basalt *in situ*. Vegetation consists of only sparse growth of sage and grass. This thin cover of plants appears to be the only reflector of radar energy on the otherwise featureless older units. This effect is demonstrated at F (Figure 11c), where a cleared field has a distinctly lower radar brightness than its surroundings. Note that the vegetation effect is most pronounced on the LHV image. The northern portion of the eastern Snake River Plain contains many young pahoehoe and aa lava flows. They are typically unweathered and free of mantling loess. The oldest Pleistocene flows have surface deposits of loess and cinders from subsequent eruptions. The strongest radar scatters are outcrops of fresh aa whose locations are shown in Figure 11d. The aa units are exceptionally bright on the cross-polarized image, a consequence of multiple reflections from the craggy, jumbled surface.

Figure 11b is a Seasat-A radar image of the western part of the eastern Snake River Plain. The brightnesses of the various units are generally similiar

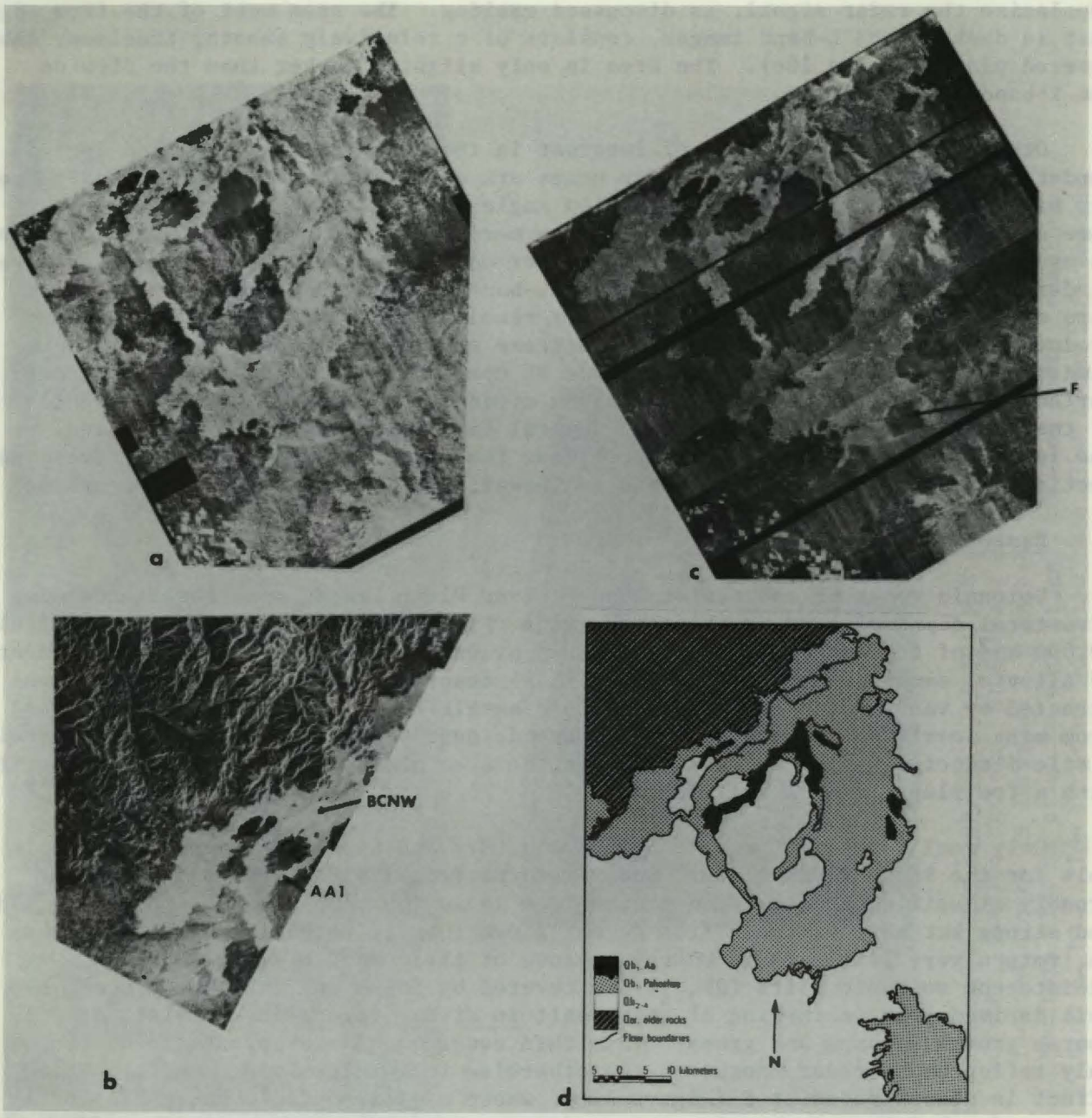

Figure 11. Eastern Snake River Plain. a) JPL LHH mosaic acquired 25 Aug. 1977 and 6 Sept. 1977. Illumination from upper left and lower right. b) Digitally correlated Seasat-A SAR image of northwest part of eastern Snake River Plain. Note brightness differences for BCNW and AA1 flows in a). c) JPL LHV mosaic acquired 25 Aug. 1977 and 6 Sept. 1977. Illumination from upper left and lower right. d) Geologic map simplified from La Point, 1977.

on the aircraft and satellite images except for the Big Crater North West (BCNW) pahoehoe flow for which the effect of incidence angle variation is particularly noticeable. The LHH aircraft image taken at 0 = 45° displays considerable mottling on the BCNW flow and distinct contrast with a nearby brighter aa flow (AA1). On the Seasat image taken at 0 = 20°, the mottling is not present and the BCNW flow actually appears brighter than AA1. Figure 12 provides, in sketch form, an explanation for this effect. The backscatter cross section σ as a function of incidence angle is much flatter for the very rough aa than for the pahoehoe of the BCNW flow. This is similar to the effect noted earlier for the hummocky pahoehoe of Pisgah lava field.

Other geomorphic features seen in the radar images include buttes, lava lakes, and lava tubes. Most of the buttes and lava lakes have a bright peripheral contour caused by collapse of their walls. Several can be seen on the west side of Figure 11a and c. Lava tubes appear as bright, curvilinear features as in Medicine Lake Highland. Part of Bear Trap Lava Tube may be seen outside the eastern corner of the cleared field at F in Figures 11a and c.

F. Newberry Volcanic Field

Newberry volcano is located about 40 km south of Bend, Oregon. The volcanic activity that built the prehistoric shield volcano probably began during the Pliocene (Peterson et al., 1965). The early flows from the volcano were basalt followed by thick sheets of rhyolite and basaltic ash. After the volcano reached its maximum size, successive eruptions of basaltic lavas resulted in the collapse of the summit. Postcaldera explosive eruptions alternated with quiet outflow to form a variety of landforms. Parasitic cinder cones, which are mostly confined to the north and south slopes of the shield, are well-preserved. All of the cones are composed of scoriaceous bombs, lapilli and basaltic cinders. Most of the area around the caldera is forest covered. The summit caldera and cinder cones are clearly visible on the Seasat SAR image (Figure 13), for the most part because of their topography. The bright region around the caldera is mostly due to the forest cover. The flows within the caldera are not distinguishable.

A zone of faults and fissures, called the Northwest Rift, runs about N 30° W from the caldera wall. Eight separate basaltic aa flows have been erupted from this rift zone. All of the flows have radiocarbon ages between 5800 ±100 and 6380 ±130 years (Chitwood, 1977). On the Seasat images, these flows are clearly visible as bright units to the upper left of Figure 13.

A large basaltic pahoehoe lava flow of questionable Holocene age has been mapped east of China Hat (Peterson et al., 1976). The flow is thickly covered with pumice from Holocene explosive eruptions from within Newberry Volcano. The pumice cover on the flow supports a pine forest; however, ropy surfaces, tumuli and primary flow surfaces are preserved at the northern terminus. China Hat is visible on the Seasat image because of its topographic expression; however, the different flow units are not clearly visible because of the vegetation cover.

The Devil's Garden is located near the center of the High Lava Plains approximately 80 km southeast of Bend. The plains form a hummocky, undulating upland region that is underlain by a thick section of Cenozoic volcanic rocks. Most of the surface shows little or no erosion (Peterson et al., 1965). The oldest rocks exposed are Pliocene andesites, dacites, and glassy rhyolites. However,

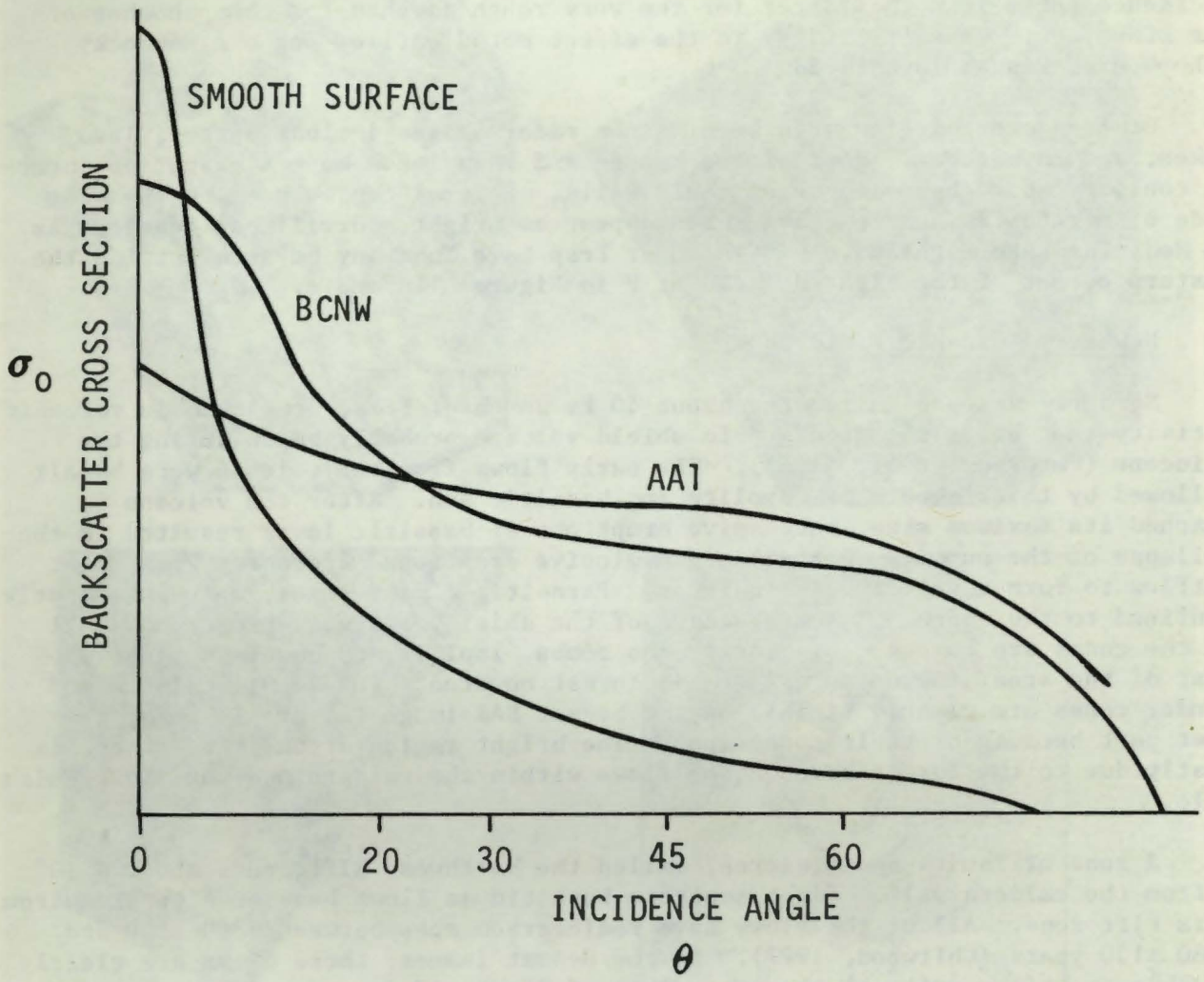

Figure 12. Schematic backscatter curves for three different surfaces showing backscatter cross section, σ_0, as a function of incidence angle θ. Note that σ_0 (AA1)$<\sigma_0$ (BCNW) for θ = 20 whereas σ_0(AA1)$>$ σ_0(BCNW) for θ = 45°.

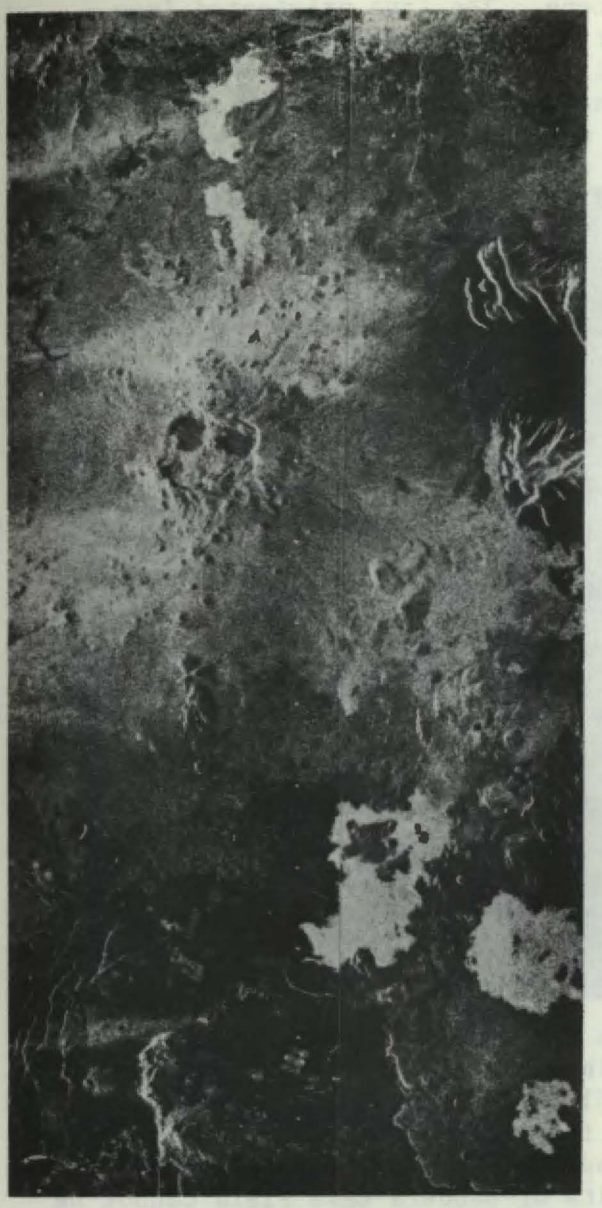

SEASAT (OP)

10km

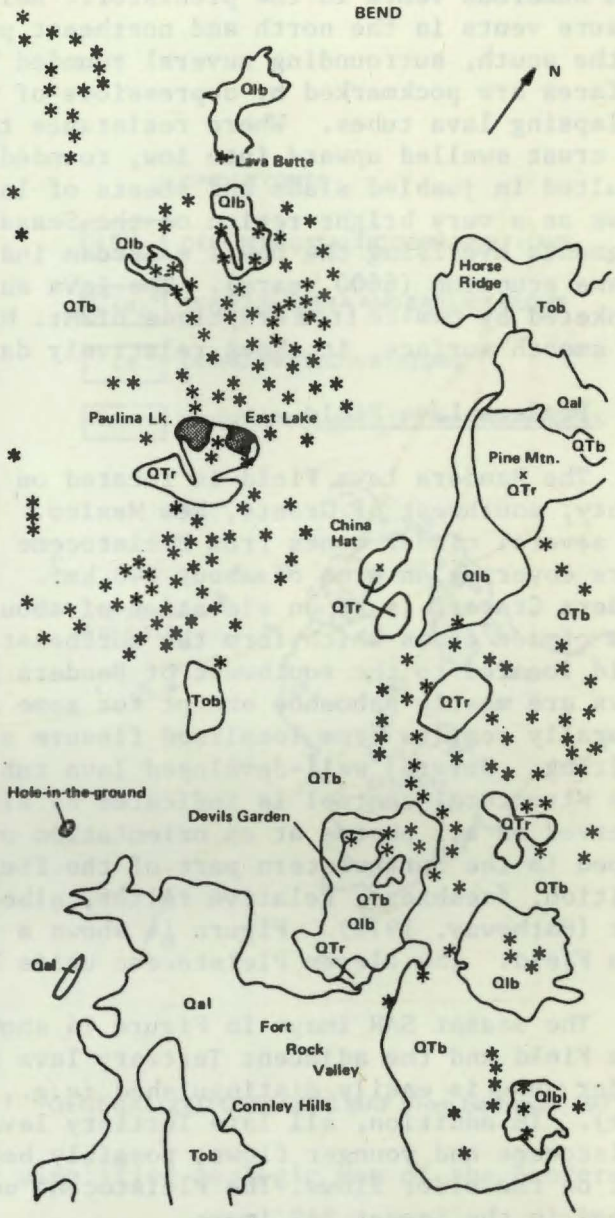

*Cinder cones

Qal : unconsolidated alluvial, dune and other deposits

Qlb : youngest flows of scoriaceous, olivine and basalt

QTb: flows and pyroclastic deposits of basaltic to rhyolitic composition

QTr: rhyolite and dacite flows, breccia and domes

Tob: basaltic and andesitic flows and tuffs (generalized from geologic map of Oregon)

Figure 13. Seasat-A SAR image and a simplified geologic map of the Newberry volcanic field region, Oregon.

basaltic eruptions predominated at the close of the Pliocene and continued through the Pleistocene. The Devil's Garden Lava Field is made of thin pahoehoe flows from numerous vents in the prehistoric Holocene. The lava originated from fissure vents in the north and northeast part of the Devil's Garden and spread to the south, surrounding several rounded hills of older rocks. The pahoehoe surfaces are pockmarked by depressions of various sizes and shapes caused by collapsing lava tubes. Where resistance to spreading of the lavas was too great, the crust swelled upward into low, rounded, cracked-open domes or tumuli which resulted in jumbled slabs and sheets of lava (Peterson et al., 1965). This flow shows as a very bright region on the Seasat SAR image. Some ashy soil and pumice fragments overlying the Devil's Garden indicate that is is older than the Mt. Mazama eruption (6600 years). The lava surface north of Devil's Garden has been blanketed by pumice from eruptions of Mt. Mazama and Newberry Volcano. Because of its smooth surface, it shows relatively dark on the Seasat image.

G. Bandera Lava Field

The Bandera Lava Field is located on the Continental Divide in Valencia County, southwest of Grants, New Mexico. The field is composed of olivine basalts and several cinder cones from Pleistocene in age to as young as a few hundred years covering an area of about 640 km^2. The rim of the largest cinder cone, Bandera Crater, is at an elevation of about 2700 m. Many of the flows originate from cinder cones which form the northeast extension of a large Tertiary volcanic field located to the southwest of Bandera Lava Field. The surfaces of the lava flows are mostly pahoehoe except for some aa and block lava units. Aa lava generally results from localized fissure eruptions and spatter cones related to faulting. Several well-developed lava tubes are found in the pahoehoe units. Some structural control is indicated by alignment of cinder cones and lineaments observed on air photos at an orientation of N 40° E. Eleven basalt units were mapped in the northwestern part of the field on the basis of stratigraphic position, freshness, relative relief, albedo, vegetative cover and soil development (Hatheway, 1971). Figure 14 shows a generalized geologic map of Bandera Lava Field. The eleven Pleistocene units have been grouped together as one unit.

The Seasat SAR image in Figure 14 shows the southwestern part of Bandera Lava Field and the adjacent Tertiary lava field. The morphology of the smallest cinder cones is easily distinguished (e.g., El Calderon: 500 m in diameter at its base). In addition, all late Tertiary lava flows can be distinguished from Pleistocene and younger flows, possibly because of soil and vegetation development on the older flows. The Pleistocene units of Bandera Lava Field cannot be mapped in the Seasat SAR image.

V. SAND DUNE FIELDS

For each of the sand dune fields which were studied, the areal extent, general pattern and geometric organization of the fields was easily recognized on the radar images. This includes (1) the differentiation between sand sheets or stringers and sand dunes, (2) areal extent and boundaries of the sand fields, and (3) the large-scale dune types which compose each dune field. Dune features which are smaller than a few resolution elements cannot be readily discerned.

10 KM

SEASAT (OP)

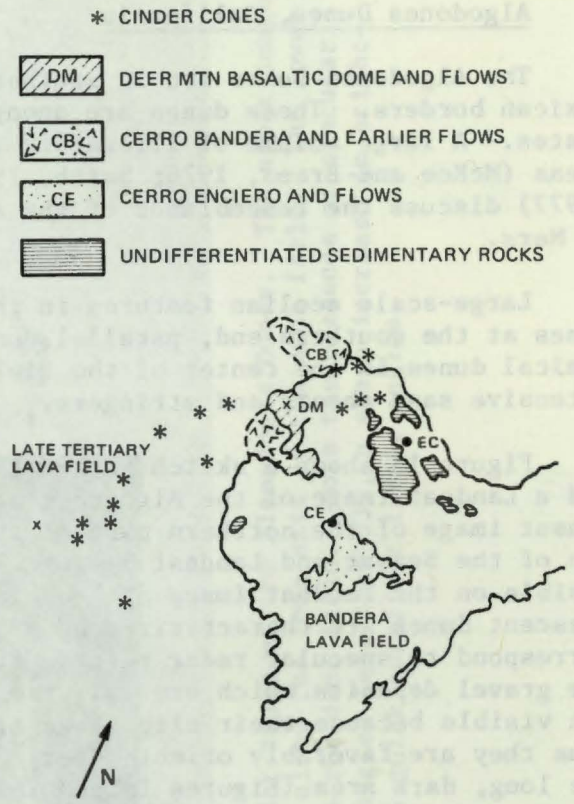

GENERALIZED GEOLOGIC MAP (from Hatheway, 1971)

Figure 14. Seasat-A SAR image and a simplified geologic map of the Bandera Flow, New Mexico

The radar backscatter from sand dunes is dominated by the specular return from the dunes' slip faces, which have slopes of less than 34°. Thus, sand dunes should show better on images with small incidence angles (less than 34° from vertical) versus intermediate incidence angles (34° to 56°). This was pointed out by Brown and Saunders (1978) in their analysis of airborne radar images of the Algodones Dunes (see Figure 15). Preliminary analysis of the radar images of some sand fields in the U.S. and Mexico is presented in this section.

A. Algodones Dunes, California

The Algodones Dunes are in southeastern California near the Arizona and Mexican borders. These dunes are among the largest active dunes in the United States. A large volume of literature is available on the dunes and surrounding areas (McKee and Breed, 1976; Smith, 1978). Cutts and Smith (1973) and Breed (1977) discuss the resemblance of the Algodones Dunes to the Hellespontus Dunes on Mars.

Large-scale aeolian features in the main dune field include giant crescent dunes at the southern end, parallel dunes on the west side and complex coalesced domical dunes in the center of the field. To the west of the dunes proper, are extensive sand sheets and stringers.

Figure 16 shows a sketch map of the prominent features, a Seasat SAR image and a Landsat image of the Algodones sand field. Figure 17 is a blowup of the Seasat image of the northern part of the field (digitially processed). A comparison of the Seasat and Landsat images shows that all the various aeolian features visible on the Landsat image are recognizable on the radar image. The giant crescent dunes are characterized by a high density of bright points, which correspond to specular radar returns from numerous dune faces. Interdune flats are gravel deposits which are quite smooth. The parallel dunes on the west side are visible because their slip faces are parallel to the path of the satellite; thus they are favorably oriented for specularly reflecting the radar signal. The long, dark area (Figures 15 and 16) east of the main axis of the dunes in the northern half corresponds to a ridge of dunes which has a steep slope facing away from the radar look direction. Thus, the return is very low because the effective incidence angle is large, eliminating the possiblity of specular return.

B. Sonora Dunes, Mexico

The Sonara Dunes are in northern Mexico southeast of the Algodones Dunes. They exhibit a considerable variety of aeolian features. McKee and Breed (1976) and McKee et al. (1977) have studied the Skylab and Landsat images of these dunes and present data on the wind regime.

Landsat and Seasat images of the Sonora Dunes are shown in Figure 18. Major features which are visible on both images include chains of star dunes in the northwest, giant crescent dunes in the east and a region of parallel wavy dunes, sand sheets and stringers on the west and south. The Pinacate volcanic field starts on the right edge of the Seasat image.

The sand dunes' features are observed on the radar image due to the variation in the density of bright specular returns. Each specular return most likely corresponds to a favorably oriented face of a small dune which is part of the giant dune. The chain of star dunes and the intradune flats are

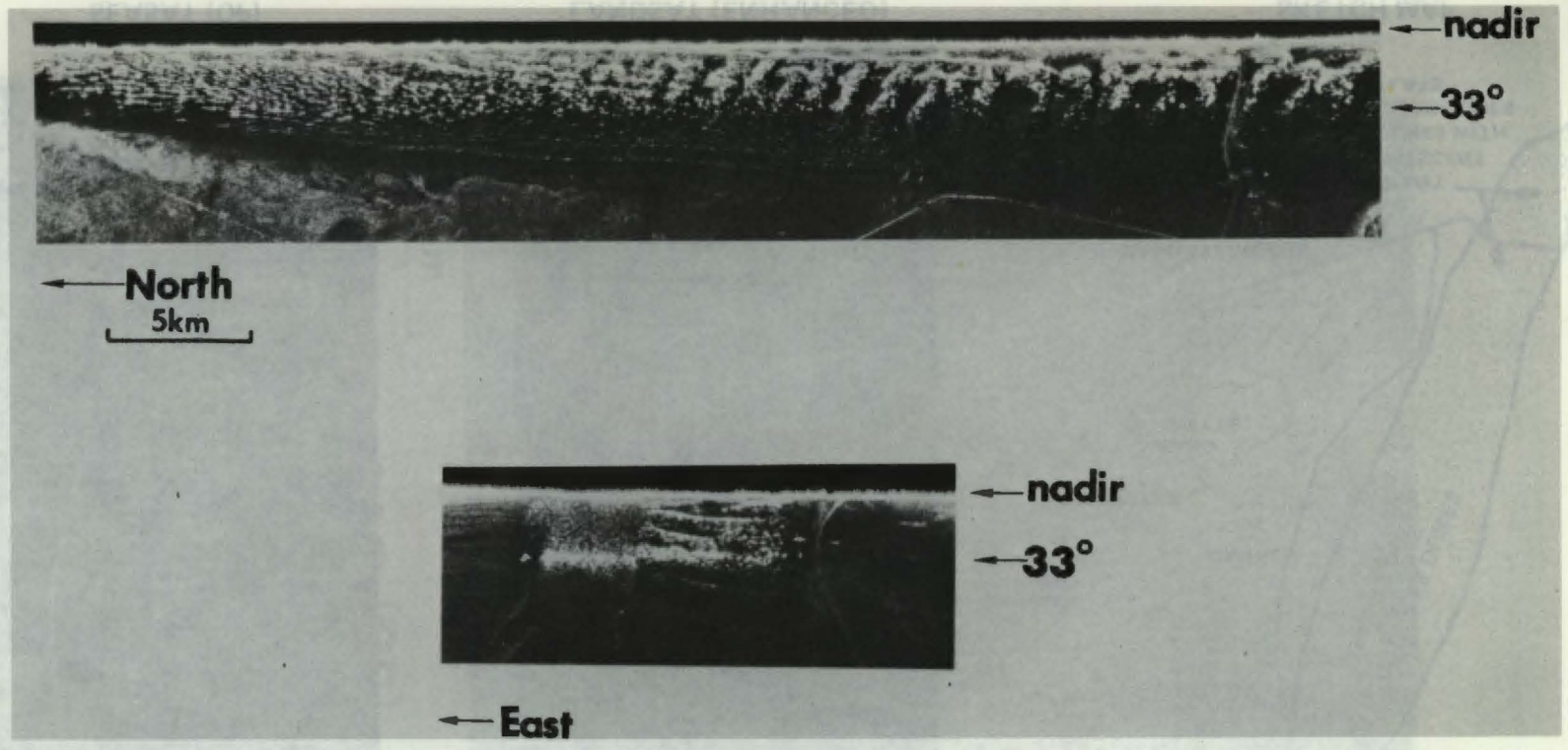

Figure 15. Airborne L-band HH radar image of the Algondones Dunes. The upper image was taken during a flight along the long axis of the dune field. The lower image was taken across the dune field. Note the presence of specular returns at incidence angles less than 33°, a sharp increase in brightness around 33°, and a quick cutoff at larger angles.

SEASAT (OP)

LANDSAT (ENHANCED)

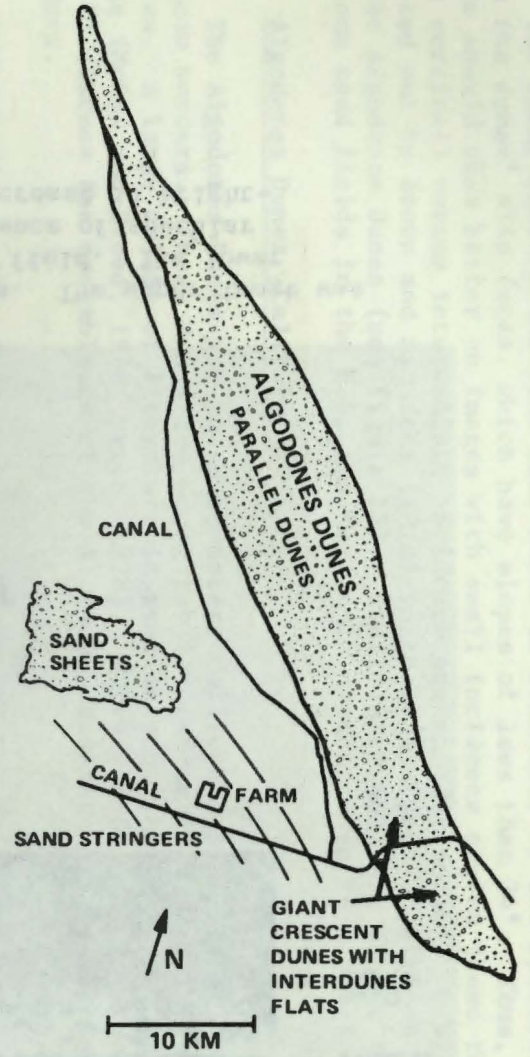

SKETCH MAP

Figure 16. Seasat-A SAR and Landsat images of the Algondones Dunes field. On the right is a sketch map of some of the most prominent features.

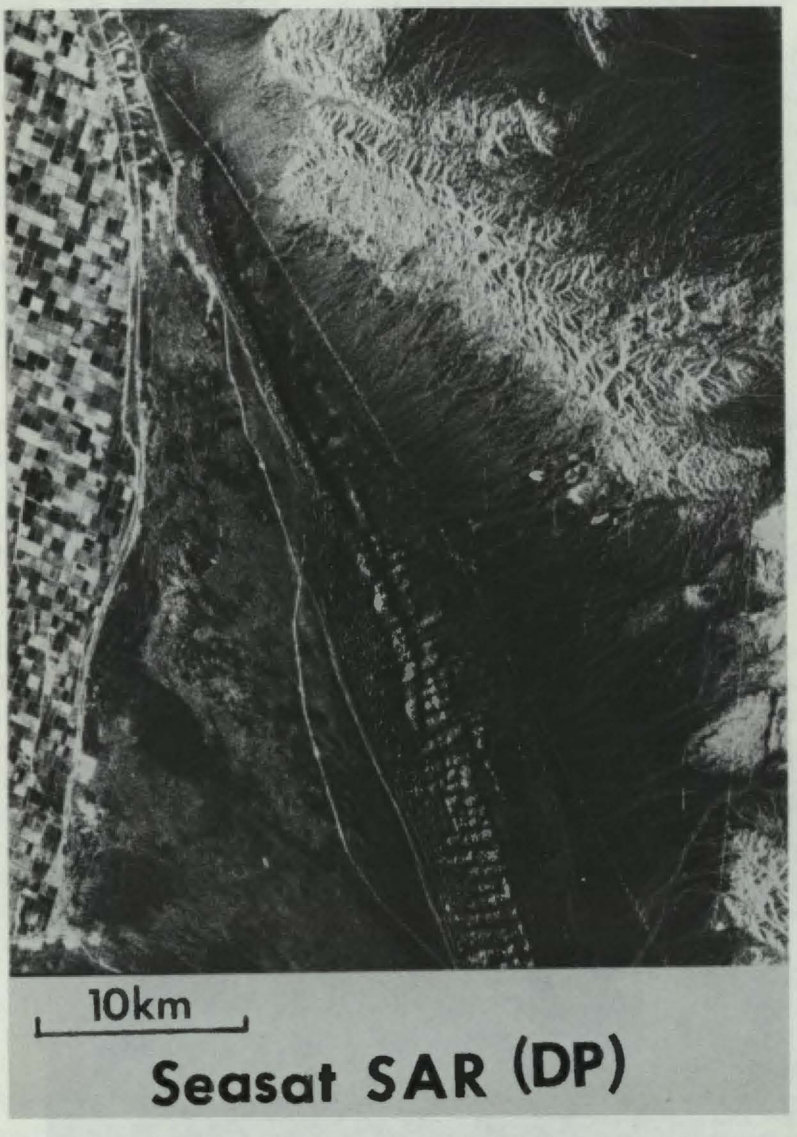

Figure 17. Blowup of the Seasat-A SAR image of the northern section of the Algondones field. This image has been digitally processed with a 25 m resolution.

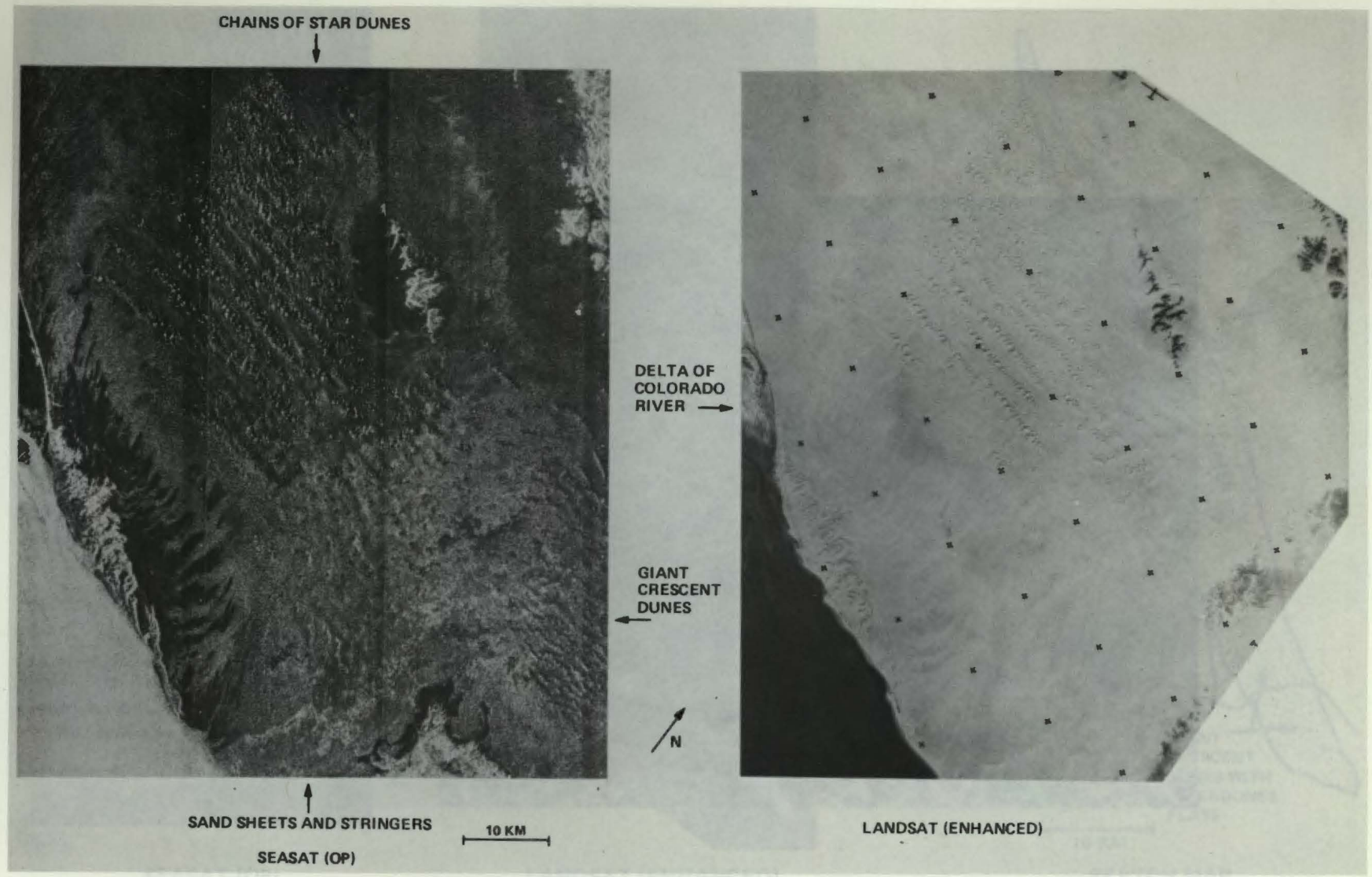

Figure 18. Seasat-A SAR and Landsat images of the Sonora desert dunes, Mexico.

clearly visible. However, it is difficult to recognize from the radar image that these are star dunes. The addition of an image with a different illumination direction would give sufficient information to infer the dune type.

C. Santa Maria Sand Dunes

The deserts of northern Mexico contain numerous small dune fields. Figure 19 shows a Seasat SAR image of a dune field near Santa Maria and Samalayuca just south of El Paso (Texas). This image is interesting because of the very high density of specular returns relative to the other Seasat images of sand dunes. This is most likely an indication of a large number of small dunes of the parallel wavy type with slip faces favorably oriented. Note also the presence of relatively high dune ridges with the corresponding dark area away from the direction of illumination. This is the same effect observed in the Algodones region.

VI. CONCLUSIONS AND RECOMMENDATIONS

Based on the limited number of sites which have been studied we can make some preliminary conclusions. In the case of volcanic fields:

(1) Volcanic features which have a relatively large topographic expression and characteristic geomorphology (cinder cones, calderas, collapse craters, etc.) are easily recognized on radar images independently of the frequency or polarization of the radar sensor. The look-angle is also not critical, except that small look-angles would lead to distortions and, in the extreme case, fold over.

(2) The identification of lava flows and differentiation between flows of different ages is best done with an L-band system (vs X- or K-band). This is simply a result of the fact that in the case of X- and K-band systems the wavelength is so small that almost all flows, as well as most surrounding terrains, look very rough to the radar.

(3) In the L-band case, it seems that the cross-polarized channel (LHV) is more sensitive than the direct polarized channel (LHH) of different lava flows.

(4) In the L-band case, younger flows are always brighter than older flows.

(5) The use of multiple frequency and multiple polarization will help in the possibility of determining the type of flow, such as aa vs pahoehoe vs blocky.

(6) For small look-angles (i.e., 20°), the interpretation of the image is harder than for large look-angles. This is due to the fact that at around 20° both quasispecular and diffuse scattering play major roles and their relative contributions cannot be determined. At large incidence angles, the diffuse component is dominant, which allows delineation of flows based on their roughness, which seems to be a very effective identifying parameter.

In the case of sand dune fields:

SEASAT (OP)

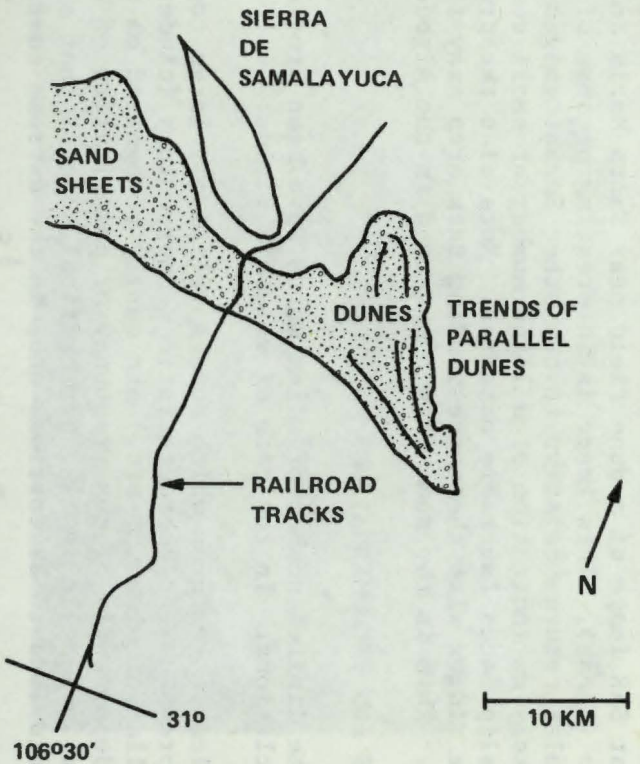

SKETCH MAP

Figure 19. Seasat-A SAR image of a sand dune field near Santa Maria in Mexico, just south of El Paso.

(1) Most of the features of sand dune fields (such as areal cover and geometric organization) can be determined.

(2) Differentiation between straight parallel dunes, wavy parallel dunes and sand sheets or stringers is possible. However, identification of distributed dune features such as barchans or star dunes requires that they subtend several resolution elements (~10) to be identifiable.

(3) It seems that small look-angles (less than 34°) might be necessary to clearly observe sand dune fields.

(4) The effect of polarization was not studied. However, the cross-polarized return should be practically nonexistent because of the specular nature of the scattering.

Based on these observations, the following preliminary recommendations can be made for VOIR:

(1) L-band is a preferred frequency. This choice is also required to avoid excessive atmospheric absorption.

(2) Direct polarization is preferred. The addition of a cross-polarized channel is useful, particularly for identifying the types of lava flows.

(3) A variable look-angle is highly desirable. The range should extend from about 20° to as large as possible, preferably more than 56°.

The above conclusions and recommendations were based on a limited set of data. Appreciably more work is still needed to further our capability of identifying and mapping lava flows and sand dune types. These recommendations based on terrestrial studies should be complemented by the results of investigations into the erosional mechanisms and weathering patterns which might be expected on Venus.

REFERENCES

Anderson, C. A., Volcanic History of Glass Mountain, Northern California, Am. Jour. Sci., 26, 485-506, 1933.

Anderson, C. A., Volcanoes of the Medicine Lake Highland, California, Univ. of California Pub. in Geol. Sci. 25, 344-422, 1941.

Barca, R. A., Geology of the Northern Part of Old Dad Mountain Quadrangle, San Bernardino Co., California, Calif. Div. Mines Geol. Map Sheet 7, 1965.

Beckman, P., and Spizzichino, A. M., Electromagnetic Scattering from Rough Surfaces, Pergamon Press, London, 1963.

Breed, C. S., Terrestrial Analogs of the Hellespontus Dunes, Mars, Icarus, 30, 326-340, 1977.

Brown, W. E., and Saunders, R. S., Radar Backscatter from Sand Dunes, NASA Tech. Memo 79729, 137-139, 1978.

Chesterman, C. W., Age of the Obsidian Flow at Glass Mountain, Siskiyou Co., California, Am. Jour. Sci., 253, 418-424, 1955.

Chitwood, L. A., Jensen, R. A., and Groh, E. A., The Age of Lava Butte, The Ore Bin, 39, 157-164, 1977.

Cutts, J. A., and Smith R. S. U., Eolian Deposits and Dunes on Mars, J. Geophys. Res., 78, p. 4139-4154, 1973.

Daily, M., Elachi, C., Farr, T., Stromberg, W., Williams, S., and Schaber, G., Application of Multispectral Radar and Landsat Imagery to Geologic Mapping in Death Valley, NASA-Jet Propulsion Lab. Pub. 78-19, 1978a.

Daily, M., Elachi, C., Farr, T., and Schaber, G., Discrimination of Geologic Units in Death Valley Using Dual Frequency and Polarization Imaging Radar Data, Geophys. Res. Letters, 5, p. 889-892, 1978b.

Daily, M., Farr, T., Elachi, C., and Schaber, G., Geologic Interpretation of Multipolarization Radar/Landsat Digital Composite Image in Death Valley, California, Photogram, Eng. Rem. Sensing, 45, 1109-1116, 1978c.

Dellwig, L. F., An Evaluation of Multifrequency Radar Imagery of the Pisgah Carter Area, California, Modern Geol., 1, 65-73, 1969.

Dellwig, L. F., and Moore, R. K., The Geologic Value of Simultaneously Produced Like and Cross-Polarized Radar Imagery, Jour. Geoph. Res., 71, 3597-3601, 1966.

Evans, D. L., Radar Observations of a Volcanic Terrain, Askja Caldera, Iceland, NASA-Jet Propulsion Lab Pub. 78-81, 42 pp. 1978.

Finch, R. H., Burnt Lava Flow in Northern California, Seit, Vulk. 15, 180-183, 1933.

Greeley, R., and King, J. S., Ed., Volcanism of the Eastern Snake River Plain, Idaho: A Comparative Planetary Geology Guidebook. Pub. by Office of Planetary Geology, NASA, 308 pp. 1977.

Greeley, R., and Iversen, J. D., Field Guide to Amboy Lava Flow, San Bernardino Co., California, in Aeolian Features of Southern California: A Comparative Planetary Geology Guidebook, Pub. by Office of Planetary Geology, NASA, 1978.

Hatheway, A., Lava Tubes and Collapse Depressions, Unpub. Ph.D. Thesis, Univ. of Arizona, 1971.

Janza, F. J., Interaction Mechanisms, Chapter 4 in Manual of Remote Sensing, R. G. Reeves Ed., Amer. Soc. of Photogram., 1975.

La Point, P. J. I., Preliminary Photogeologic Map of the Eastern Snake River Plain, Idaho, USGS Misc. Field Studies Map MF-850, 1977.

Lefebvre, R. H., Mapping in Craters of the Moon Volcanic Field, Idaho, with Landsat (ERTS) Images. Proc. of Tenth Int'l. Symp. on Rem. Sensing of Env., 951-963, 1976.

MacDonald, G. A., Geology of the Cascade Range and Modoc Plateau, Calif. Div. Mines Geol. Bull. 190: 65-96, 1966.

MacDonald, H. C., Geologic Evaluation of Radar Imagery from the Darien Province, Panama, Modern Geology, 1, 1-63, 1969.

Malin, M. C., Evans, D. L., and Elachi, C., Imaging Radar Observations of Askja Caldera, Iceland, Geoph. Res. Letters. 5, 931-933, 1978.

McCauley, J. R., Surface Configuration as an Explanation for Lithology Related Cross-Polarization Radar Image Anomalies, Univ. of Kansas Center for Research, Inc., Tech. Rept. 177-36, 54 pp., 1972.

McKee, E. D., and Breed, C. S., Sand Seas of the World, in ERTS-1, A New Window on Our Planet, USGS Prof. Paper 929, 1976.

McKee, E. D., Breed, C. S., and Fryberg, S. G., Desert Sand Seas, in Skylab Explores the Earth, NASA SP-380, 5-48, 1977.

Parker, R. B., Recent Volcanism at Amboy Crater, San Bernardino Co., California, Calif. Div. Mines Geol., Spec. Rept. 76, 23 pp., 1963.

Peterson, N. V., Groh, E. A., Taylor, E. M., and Stensland, D. E., Geology and Mineral Resources of Deschutes County, Oregon, State of Oregon Dept. of Geology and Mineral Industries Bulletin 89, 66 pp. 1976.

Peterson, N. V., Groh, E. A., Newhouse, C. J., State of Oregon Lunar Geological Field Conference Guidebook, State of Oregon Dept. of Geology and Mineral Industries Bulletin 57, 51 pp., 1965.

Russell, I. C., Geology and Water Resources of the Snake River Plain of Idaho, USGS Bull. 199, 192 pp., 1902.

Ruck, G. T., Editor, Radar Cross-Section Handbook, Plenum Press, N.Y., 1970.

Sabins, F. F., Jr., Remote Sensing, Principles and Interpretation, W. H., Freeman and Co., San Francisco, 426 pp., 1978.

Schaber, G. G., Berlin, G. L., and Brown, W. E., Jr., Variations in Surface Roughness Within Death Valley, California, Geologic Evaluation of 25 cm Wavelength Radar Images, Geol. Soc. Am. Bull. 87, 29-41, 1976.

Schaber, G. G., Elachi, C., and Farr, T., Remote Sensing Data of SP Mountain and SP Lava Flow in North Central Arizona, Remote Sensing of the Environment, in press, 1979.

Valenzuela, G. R., Depolarization of EM Waves by Slightly Rough Surfaces, IEEE Trans. Ant. and Prop., AP-15, p. 552, 1967.

Wise, W. S., Geologic Map of the Pisgah and Sunshine Cone Lava Fields, NASA Tech. Letter NASA-11, 1966.

Wise, W. S., Preliminary Geologic Map of Kel-Baker Volcanic Field, unpublished, personal communication, 1978.

ACKNOWLEDGEMENT

The authors acknowlege the constructive comments and help from their colleagues at JPL, in particular Dr. J. Ford and Ms. D. Evans. The effort on volcanic field mapping with radar was conducted in conjunction with efforts at USGS in Flagstaff (G. Schaber).

The research described in this paper was carried out by the Jet Propulsion Laboratory, California Institute of Technology, under NASA Contract No. NAS7-100.